Southern hemisphere circumpolar wavenumber-4 pattern simulated in SINTEX-F2 coupled model

Article

Updated Version

Accepted version with figures

Southern Hemisphere Circumpolar Wavenumber-4 Pattern Simulated in SINTEX-F2 Coupled Model

Balaji Senapati[1,2], Yushi Morioka[3], Swadhin K. Behera[3], and Mihir K. Dash[1]

[1] Centre for Ocean, River, Atmosphere and Land Sciences, Indian Institute of Technology Kharagpur, Kharagpur, West Bengal, India

[2] Department of Meteorology, University of Reading, Reading, UK

[3] Application Laboratory, VAiG, Japan Agency for Marine-Earth Science and Technology, Yokohama, Kanagawa, Japan

Corresponding author: Mihir K. Dash (mihir@coral.iitkgp.ac.in)

Key Points:

- First attempt to successfully simulate the wavenumber-4 pattern of Southern Ocean SST using a coupled model, uncovering the underlying physical processes.
- Southwestern subtropical Pacific SST plays a crucial role in generating SST wavenumber-4 pattern via circumpolar atmospheric variability.
- The ocean mixed layer is found to be important for the growth and decay of the SST pattern.

Keywords: Wavenumber 4, SINTEX-F2 coupled model and sensitivity experiments, Mixed layer heat budget, air-sea interaction, SST, Southern Hemisphere subtropics and mid-latitude

ORCID

Balaji Senapati: https://orcid.org/0000-0001-5029-9731

Yushi Morioka: https://orcid.org/0000-0002-2709-4911

Swadhin K. Behera: https://orcid.org/0000-0001-8692-2388

Mihir K. Dash: https://orcid.org/0000-0003-1426-7200

Abstract

Interannual sea surface temperature (SST) variations in the subtropical-midlatitude Southern Hemisphere are often associated with a circumpolar wavenumber-4 (W4) pattern. This study is the first attempt to successfully simulate the SST-W4 pattern using a state-of-the-art coupled model called SINTEX-F2 and clarify the underlying physical processes. It is found that the SST variability in the southwestern subtropical Pacific plays a key role in triggering atmospheric variability and generating the SST-W4 pattern during austral summer (December-February). In contrast, the tropical SST variability has very limited effect. The anomalous convection and associated divergence over the southwestern subtropical Pacific induce atmospheric Rossby waves confined in the westerly jet. Then, the synoptic disturbances circumnavigate the subtropical Southern Hemisphere, establishing an atmospheric W4 pattern. The atmospheric W4 pattern has an equivalent barotropic structure in the troposphere, and it interacts with the upper ocean, causing variations in mixed layer depth due to latent heat flux anomalies. As incoming climatological solar radiation goes into a thinner (thicker) mixed layer, the shallower (deeper) mixed layer promotes surface warming (cooling). This leads to positive (negative) SST anomalies, developing the SST-W4 pattern during austral summer. Subsequently, anomalous entrainment due to the temperature difference between the mixed layer and the water below the mixed layer, anomalous latent heat flux, and disappearance of the overlying atmospheric W4 pattern cause the decay of the SST-W4 pattern during austral autumn. These results indicate that accurate simulation of the atmospheric forcing and the associated atmosphere-ocean interaction is essential to capture the SST-W4 pattern in coupled models.

Plain Language Summary

In the subtropical-midlatitude Southern Hemisphere, we often observe year-to-year fluctuations in sea surface temperature (SST) linked to a specific pattern known as wavenumber-4. This study represents the first successful attempt to simulate this temperature pattern using a climate emulator called SINTEX-F2, allowing us to uncover its physical processes. Our research reveals that SST variations in the southwestern subtropical Pacific (SWSP) play a pivotal role in generating the wavenumber-4 pattern in the atmosphere, subsequently influencing SST during austral summer. Interestingly, this pattern is almost independent of tropical SST variability.

The process starts with heating in the SWSP, causing atmospheric disturbances. This leads to an undulation in mid-latitude atmospheric flow, evolving into a well-established global Rossby wave with four positive (negative) loading centers, forming a wavenumber-4 pattern. This atmospheric wave interacts with the ocean's surface, leading to heat exchange between the atmosphere and the upper ocean. In turn, it influences the depth of the mixed layer in the upper ocean, which receives solar energy. When solar energy penetrates into a shallower (deeper) mixed layer, it warms (cools) the mixed layer effectively, resulting in higher (lower) SSTs. Afterward, the energy exchange between the mixed layer and the deep ocean contributes to the decay of the SST pattern.

1 Introduction

Oceans cover more than 80% of the surface area in the Southern Hemisphere and primarily affect the rainfall variability over the landmasses, hence impacts the regional hydrology, agriculture, drinking water, economy and livelihood of the society. Further, rainfall deficit over these regions is closely associated with the climate variability over subtropical-midlatitude oceans (Barros & Silvestri, 2002; Behera & Yamagata, 2001; Diaz et al., 1998; Paegle & Mo, 2002; C. Reason, 1999, 2001; Taschetto & Wainer, 2008). The linkage of these rainfall variabilities with tropical climate variability has been extensively studied in recent decades (Ashok et al., 2003; Grimm et al., 2000; Richard et al., 2000). However, the dynamics of the subtropical-midlatitude oceans and their influence on the subtropical climate have drawn little attention until the 21st century. One of the major factors affecting the subtropical climate is sea surface temperature (SST) due to its interaction with the overlying atmosphere. The SST variability in the subtropical-midlatitude Southern Hemisphere has the potential to impact global climate directly or indirectly through the dynamics of the ocean, atmosphere, and climate on interannual to decadal timescales (Liu & Alexander, 2007). Thus, understanding the physical mechanisms of the interannual SST variability in the subtropical-midlatitude Southern Hemisphere is crucial in improving the knowledge of the underlying dynamics of climate variability.

The subtropical-midlatitude SST in the Southern Hemisphere reaches its peak during austral summer (December-February), shows the largest interannual variability because of intense insolation and shallower mixed layer depth (MLD), which facilitates interaction with the overlying atmosphere and upper ocean (Suzuki et al., 2004). The major SST variabilities over the subtropical regions are closely associated with the subtropical highs, called Subtropical Dipole (Behera & Yamagata, 2001; Fauchereau et al., 2003; Hermes & Reason, 2005; Morioka, Ratnam, et al., 2013; Venegas et al., 1997). Possible sources of the variations in the subtropical high are internal or connected to El Niño/Southern Oscillation (ENSO), Indian Ocean Dipole (IOD) and Southern Annular Mode (SAM) (Anila & Gnanaseelan, 2023; Crétat et al., 2018; Morioka et al., 2012; Morioka, Tozuka, et al., 2013; Rodrigues et al., 2015). For example, ENSO-induced Pacific South American pattern (Mo & Paegle, 2001) shifts the St. Helena High meridionally and hence generates the Subtropical Dipole in the South Atlantic (Rodrigues et al., 2015). Similarly, the Subtropical Dipole in the southern Indian Ocean develops due to variation in Mascarene High influenced by ENSO, IOD and SAM (Anila & Gnanaseelan, 2023; Crétat et al., 2018; Morioka, Tozuka, et al., 2013). Further, in the absence of tropical SST variability, Rossby waves related to the SAM can generate Subtropical Dipoles by modulating sea level pressure anomalies in the mid-latitude Southern Hemisphere (Morioka et al., 2014a). Synchronization of these Subtropical Dipoles in each ocean basin turns into a global wavenumber-3 pattern in the subtropical Southern Hemisphere (Wang, 2010).

Despite these efforts, few studies have discussed the interannual SST variability over the entire subtropical Southern Hemisphere (Wang, 2010; Senapati, Dash, et al., 2021). This might be due to the paucity of observations over the regions (see Fig. 1 in Morioka et al. (2013)). The substantial increase in the SST observations after 1980s helps enhance confidence in studying the SST variability over the regions. Recently, a circumpolar wavenumber-4 (W4) pattern has been reported in the atmospheric circulation (Senapati, Deb, et al., 2021), which can influence the ocean (Senapati, Dash, et al., 2021) as similar to a wavenumber-3 pattern (Wang, 2010). Wang (2010) discussed the covarying Subtropical Dipoles in each basin of the Southern Hemisphere and suggested it as the wavenumber-3 pattern. Nevertheless, Senapati et al. (2021a) investigated the interannual SST variability, focusing on the subtropical- midlatitude Southern Hemisphere, and reported an SST-W4 pattern for the first time. SST-W4 pattern is different from the wavenumber-3 pattern in many aspects, including location and the number of centres of actions, generation dynamics (Wang, 2010; Senapati, Dash, et al., 2021), impacts (Senapati, Dash, et al., 2021), and linkage of extra-subtropical regions (Morioka et al., 2014b; Senapati, Dash, et al., 2021). The wavenumber-3 pattern (1st EOF mode of the subtropical SST) is generated mainly due to variations in horizontal wind components indepdent of ENSO and SAM (Wang, 2010). In contrast, the SST-W4 pattern (2nd EOF mode) develops only due to meridional wind variability (Senapati, Dash, et al., 2021).

The SST-W4 pattern is suggested to be phase-locked during austral summer and occurs even in the absence of other climate variabilities. It is noted that thermodynamic feedbacks between meridional wind, surface heat flux, and mixed layer mainly cause the SST-W4 pattern. The SST-W4 pattern also undergoes a decadal variability and impacts the precipitation over Southern continents (Senapati et al., 2022). The SST footprints of the decadal variability of the South Pacific Meridional Mode (SPMM; (Zhang et al., 2014)) creates an ideal environment for the frequent occurrence of positive/negative type of the SST-W4 pattern, which results in the decadal modulation of the SST-W4 pattern after two years (Senapati et al., 2022). The SPMM, which drives the decadal variability of SST-W4 (Senapati et al., 2022), has been considered as a precursor to ENSO dynamics (Larson et al., 2018; You & Furtado, 2018). However, the tropical connection in the development of SST-W4 is lacking.

Nevertheless, the detailed air-sea interaction processes involved in the generation, growth, and decay of the SST-W4 pattern are not well investigated. In other words, how does the wind influence the MLD change and modulate the SST anomalies? Is the MLD change due to the wind stirring effect, thermal buoyancy effect, or both? If so, then what is their individual contribution to the MLD variability? The roles of wind, surface heat flux, and mixed layer variations in developing the SST-W4 pattern require thorough investigation. Also, Senapati, Dash, et al. (2021) suggested that the SST-W4 pattern decays because of the thermodynamic decoupling between the upper ocean and the overlying atmosphere and subsequent cut-off from the source. The ocean's role is not considered in the decaying phase and is essential to consider while investigating the SST variability, especially over the subtropics (Morioka et al., 2011, 2012; Morioka, Ratnam, et al., 2013). Because of the very limited availability of observation datasets, a coupled general circulation model (CGCM) is required to explore the air-sea interaction processes in detail during the growth and decay phases of the SST-W4 pattern.

Furthermore, it is suggested that the convective activity over the southwestern subtropical Pacific (SWSP) is instrumental in generating atmospheric W4 (Senapati, Deb, et al., 2021), which later produces the SST-W4 pattern. The root cause of the convective activity over the SWSP, which acts as a Rossby wave source, remains unclear. Identifying the possible sources of the convective activity is of great importance in understanding and predicting the SST and atmospheric W4 patterns.

This research aims to investigate the seasonal evolution of the SST-W4 pattern both qualitatively and quantitatively using the output of 300-yr pre-industrial control (CTL) simulation from a CGCM. We also performed a series of 100-yr sensitivity experiments to clarify the possible sources of the convective activity over the SWSP in generating SST and atmospheric W4 patterns. The structure of this document is as follows. Section 2 briefly describes the model, the data used, and methodology employed in this investigation. Section 3 discusses the results comprising the following four subsections. Subsection 3.1 validates the performance of CGCM in simulating the SST-W4 pattern in the subtropical-midlatitude Southern Hemisphere. Subsection 3.2 examines the air-sea interaction processes that contribute to the growth and decay of the SST-W4 pattern. The connection between SST and the atmosphere, along with the associated generation mechanisms, is described in Subsection 3.3. Subsection 3.4 discusses the respective roles of the tropics and the SWSP in generating SST and atmospheric W4 patterns. Finally, the study is summarized and discussed in Section 4.

2 Model, Data and Methods

2.1 CGCM and data

The physical processes involved in the SST-W4 pattern are analyzed using a CGCM, namely the Scale Interaction Experiment-Frontier Research Center for Global Change 2 (SINTEX-F2; Masson et al., 2012), which is a subsequent version of the SINTEX-F1 (Luo et al., 2005). Previous studies demonstrated reasonable performance of the model in simulating the observed seasonal and interannual SST variability in the subtropical-midlatitude Southern Hemisphere (Doi et al., 2016; Morioka et al., 2011, 2012, 2014a, 2015; Morioka, Ratnam, et al., 2013). This CGCM comprises of (i) the fifth-generation atmospheric general circulation model 5 (ECHAM5; developed from the atmospheric model of the European Centre for Medium-Range Weather Forecasts (ECMWF) with a parameterization package designed at Hamburg) atmospheric model by Roeckner et al. (2003), (ii) the Nucleus for European Modeling of the Ocean 3 (NEMO3) ocean-sea ice model by Madec (2008) and (iii) the Ocean-Atmosphere-Sea-Ice-Soil 3 (OASIS3) coupler by Valcke (2006). The atmospheric grid comprises a T106 Gaussian horizontal grid (i.e., 1.125° × 1.125°) and 31 vertical levels. NEMO3 includes the Louvain-la-Neuve Sea Ice Model 2 (LIM2; Fichefet & Maqueda, 1997) and features an ORCA05 tripolar horizontal grid (i.e., 0.5° × 0.5°) with 31 vertical levels (Gurvan Madec & Imbard, 1996). NEMO3 employs a turbulent kinetic energy closure model to calculate vertical eddy viscosity and diffusivity in the ocean (Gurvan Madec et al., 1998). To represent the effects of diapycnal mixing on ocean salinity and temperature, NEMO3 utilizes the double-diffusive mixing model established by Merryfield et al. (1999). The OASIS3 coupler (Valcke, 2006) exchanges freshwater, heat, and air-sea momentum fluxes every 2 hours between NEMO3 and ECHAM5. Additional flux corrections using reanalysis products or observational data are omitted, allowing the ocean-atmospheric states in the model to evolve freely. The ocean model is initialized with annual mean salinity and temperature data from the World Ocean Atlas 1998 (https://psl.noaa.gov/data/gridded/data.nodc.woa98.html). A 300-yr CTL simulation was performed with pre-industrial radiative forcings. The first 30 years of the simulations are excluded from the analysis to account for the time required for the ocean to adjust to the inter-annually varying atmospheric forcing (Morioka & Behera, 2021). Model results are validated using monthly mean SST data from Hadley Centre Global Sea Ice and Sea Surface Temperature (HadISST; Rayner et al., 2003) dataset with a 1°×1° spatial resolution from 1979 to 2018. Different climate indices such as the Oceanic Niño Index (ONI; Trenberth, 1997), Indian Ocean Dipole (IOD; Saji et al., 1999) index, South Atlantic Subtropical Dipole (SASD; Morioka et al., 2011) index, South Pacific Subtropical Dipole (SPSD; Morioka, Ratnam, et al., 2013) index and Indian Ocean Subtropical Dipole (IOSD; Behera & Yamagata, 2001) index are calculated in CGCM outputs to verify their connection with the SST-W4 pattern.

2.2 Sensitivity experiments

Two potential sources can create SST and atmospheric W4 patterns: (i) tropical SST variability and (ii) the SWSP SST variability. In order to identify the actual source, two SST nudging experiments are conducted using the SINTEX-F2 model. In these experiments:

(i) The model's SST in the tropical region (25°S-25°N) is nudged to the monthly climatological SST of the control simulation, referred to as the 'noTropics' experiment.

(ii) The model's SST in the SWSP region (150°E-160°W, 50°-10°S) is nudged to the monthly climatological SST of the control simulation, referred to as the 'noSWSP' experiment.

A large negative feedback (-2400 W m^{-2} K^{-1}) is added to the surface heat flux to restore the upper 50m mixed layer temperature within one day (Morioka et al., 2014b). The gaussian method is applied at the boundaries within 5° of the SST nudging area for smoothing. We integrated these experiments for 100 years, from which the last 70 years are used for the analysis after removing the initial 30 years to account the ocean's adjustment to the atmospheric forcing (Morioka & Behera, 2021). It is important to note that the surface heat flux correction in the SST-nudging experiments tends to significantly reduce the coupled interactions and variability in the corrected region. In other words, we can scrutinize the impact of SST variability in each nudging area on the

SST and atmospheric W4 patterns by subtracting the results of the CTL and SST-nudging experiments.

2.3 Statistical analysis

We calculated the monthly anomalies at all grid points for every variable by removing the corresponding monthly climatology after detrending it using the least square fit. The cost function of a variable ‘C($=\sum_{i=1}^{n}(y_i - f(x_i))^2$)’, is minimized using the least square approach to generate the best-fit function, where, y_i, x_i, and $f(x_i)$ are dependent, independent variable, and best-fit function, respectively. Following Senapati et al. (2021a), the SST-W4 pattern is captured by employing the Empirical Orthogonal Function (EOF) analysis over the subtropical and midlatitudes in the Southern Hemisphere (55°S–20°S). Further, North criteria (North et al., 1982) was used to test the significance and independency of the EOF modes. In this method, the standard error $\left[\Delta\lambda = \lambda\sqrt{\frac{2}{N}}\right]$ of the associated eigenvalues (λ) was computed by using degrees of freedom (N) present in the dataset. If the sampling error (i.e., $\Delta\lambda$) of an eigenvalue ‘λ’ is shorter than the gap between λ and the eigenvalue closest to it then ‘λ’ is considered to be independent, else otherwise. The role of atmosphere in generating the SST-W4 pattern is validated using Maximum Covariance Analysis (MCA) over the region (Senapati, Dash, et al., 2021). The MCA is a singular value decomposition approach that uses two variables' cross-covariance matrix. Since the SST-W4 pattern peaks during austral summer (Senapati, Dash, et al., 2021), singular value decomposition is applied to austral summer (December-February). Results from left (right) singular vectors correspond to the covarying pattern of the first (second) variable during austral summer. The temporal pattern is generated by projecting the corresponding pattern on the original detrended anomalous data (consisting of all calendar months).

2.4 Rossby wave source

We calculated the source of Rossby waves associated with SST and atmospheric W4 patterns (Jianchun Qin & Robinson, 1993; Sardeshmukh & Hoskins, 1988; Senapati, Deb, et al., 2021) using the following equation:

$$\text{Rossby Wave Source (RWS)} = -(\zeta + f)\nabla.V_\lambda - V_\lambda.\nabla(\zeta + f) \qquad (1),$$

where 'f' represents planetary vorticity, 'V_λ'denotes divergent wind, and 'ζ' represents relative vorticity. The first term on the right-hand side of Eq. (1) indicates the vortex stretching by eddies, while the second term corresponds to the advection of absolute vorticity by the divergent wind.

2.5 Rossby wave activity flux

To iilustrate the Rossby wave activities, two-dimensional Rossby wave activity flux (WAF; Takaya & Nakamura, 1997, 2001) is estimated from the subtropics to the polar region using the following equation:

$$WAF = \frac{p}{2|\bar{U}|} \times \begin{Bmatrix} \bar{u}\left({\Psi'_x}^2 - \Psi'\Psi'_{xx}\right) + \bar{v}\left(\Psi'_x\Psi'_y - \Psi'\Psi'_{xy}\right) \\ \bar{u}\left(\Psi'_x\Psi'_y - \Psi'\Psi'_{xy}\right) + \bar{v}\left({\Psi'_y}^2 - \Psi'\Psi'_{yy}\right) \end{Bmatrix} \qquad (2),$$

where $p = \left(\frac{pressure}{1000\ hPa}\right)$, Ψ and $|\bar{U}|$ represent the stream function and magnitude of horizontal wind vector U(u,v), respectively. Variables with bar, prime and subscript denote climatology, perturbation, and partial derivatives, respectively. The regions of weak zonal wind or easterly wind are omitted to diagnose the WAF (Takaya & Nakamura, 2001). The emergence (depletion) of WAF aligns with the generation (dissipation) of Rossby waves. The WAF is defined within the constraints of the quasi-geostrophic approximation, making it challenging to characterize the flux near the equator. Given that the Rossby waves stem from vorticity disturbances related to thermal or orographic influences (Brian J Hoskins & Karoly, 1981), we have opted to utilize the divergence (convergence) of horizontal upper tropospheric winds instead to describe potential generators of Rossby waves in this context.

2.6 Mixed layer heat budget

To investigate the air-sea interaction mechanisms that generate the SST-W4 pattern, we conducted a budget analysis of the mixed layer temperature (T_m; MLT) tendency over both positive and negative SST anomaly poles in the subtropical-midlatitude Southern Hemisphere (Morioka et al., 2011, 2012; Morioka, Ratnam, et al., 2013). This analysis involves the following equation:

$$\frac{\partial T_m}{\partial t} = \frac{Q_{net} - q_d}{\rho c_p H} - \mathrm{u}_m . \nabla T_m - \frac{\Delta T}{H} w_e + Res. \qquad (3).$$

The terms on the right-hand side of Eq. (3) represent various components, including the heat flux at the air-sea interface (first term), horizontal advection (second term; both zonal and meridional), entrainment (third term), and residual (fourth term). In the first term, Q_{net} represents the net heat flux at the ocean surface (NSHF; i.e., a sum total of net shortwave radiation (NSW), sensible heat flux (SHF), net longwave radiation (NLW), and latent heat flux (LHF)), q_d is the downward radiative heat flux at the bottom of the mixed layer (Paulson & Simpson, 1977), ρ (=1027 kg/m^3) is the average density of ocean water, and c_p (=4187 JK^{-1}kg^{-1}) is specific heat capacity of the ocean. q_d is computed by following,

$$q(z) = q(0)\left[Re^{\left(\frac{z}{\gamma_1}\right)} + (1-R)e^{\left(\frac{z}{\gamma_2}\right)}\right] \quad (4),$$

where, $q(0)$ and $q(z)$ represent the shortwave radiation at the surface and downward radiative heat flux at depth ‘z’, respectively. In our study, we adopt water type 1B, with constants γ_1=1, γ_2=17, and R=0.67 (Dong et al., 2007). The MLD (H) is computed based on the 0.5 °C temperature criteria, defined as the level where the temperature reduces by 0.5 °C compared to the SST. Similar results are obtained when MLD is calculated using a 0.125 kg m^{-3} density criteria (the level where the potential density increases by 0.125 kg m^{-3} to that at the surface). Notably, q_d is only 5% of the shortwave radiation penetrating the surface, even under the thinnest MLD conditions during the austral summer and is therefore negligible compared to Q_{net} (Morioka et al., 2012). The average horizontal velocity in the mixed layer is indicated by u_m in the second term. In the third term, ΔT (= $T_m - T_{-H-20m}$) denotes the temperature difference between MLD and entrained water (i.e. water at 20 m below the mixed layer base; Yasuda et al., 2000). Furthermore, the entrainment velocity (w_e) is defined as (Qiu & Kelly, 1993; Kraus & Turner, 1967),

$$w_e = \frac{\partial H}{\partial t} + \nabla.(\mathrm{u}_m H) \quad (5).$$

The "Res." term (i.e., residual) encompasses oceanic diffusion and additional processes with high-frequency variability.

2.7 Monin-Obukhov depth

Generally, the mixed layer is shallower during austral summer compared to other seasons in the subtropics. In this case, the change in the MLD is primarily attributed to wind stirring and surface heat fluxes rather than subsurface ocean processes beneath the mixed layer (Morioka, Ratnam, et al., 2013). To assess the contribution of each term to MLD variability, we estimate the Monin-Obukhov depth (H_{MO}),

$$H_{MO} = \frac{m_0 u_*^3 + \frac{\alpha g}{\rho c_p}\int_{-H_{MO}}^{0} q(z)dz}{\frac{\alpha g}{2\rho c_p}(Q_{net} - q_d)} \qquad (6)$$

(Qiu & Kelly, 1993; Kraus & Turner, 1967; Morioka et al., 2011, 2012; Morioka, Ratnam, et al., 2013). Here, m_0 (=0.5) is a coefficient of wind stirring (Davis et al., 1981), and u_* is the frictional velocity $\left[u_* = \sqrt{\frac{\rho_a C_D u_{10}^2}{\rho}}\right]$, where ρ_a (=1.3 kg/m^3) is air density, C_D (=0.000125) is the drag coefficient, and u_{10} is the 10 m wind speed. Additionally, g (=9.8 m s^{-1}) represents the acceleration due to gravity, α (=0.00025 °C^{-1}) denotes the coefficient of thermal expansion in water and $q(z)$ represents the downward solar insolation calculated using Eq. (5). Following the approach of Morioka et al. (2011, 2012, 2013), the interannual variability of H_{MO} is evaluated by

$$\delta(H_{MO})\left[\equiv \delta\left(\frac{m_0 u_*^3 + q_*}{Q_*}\right)\right] = \frac{m_0 \delta(u_*^3)}{\overline{Q_*}} + \frac{\delta q_*}{\overline{Q_*}} - \frac{\delta Q_*\left(m_0\overline{u_*^3} + \overline{q_*}\right)}{\overline{Q_*^2}} + Res. \qquad (7),$$

where $q_* = (\rho c_p)^{-1}\alpha g \int_{-H_{MO}}^{0} q(z)\, dz$ represents the effective penetrative radiation and $Q_* = (2\rho c_p)^{-1}\alpha g(Q_{net} - q_d)$ is the effective buoyancy forcing. The overbar and $\delta(\,)$ represent the climatology and their monthly anomaly, respectively. The first term and the sum of the second and third terms on the right side of Eq. (7) depict the contribution of wind stirring anomaly and net surface heat flux anomaly to the interannual changes in H_{MO}, respectively.

3 Results

3.1 Model validation

Before investigating the generation mechanism of the SST-W4 pattern in detail, we first assess the ability of the SINTEX-F2 to capture this pattern by comparing it with the observed data. Please note that we use the HadISST during 1979-2018 as observed data in our study. The results from both HadISST and SINTEX-F2 are presented in the left and right panels of Fig. 1, respectively. The second EOF mode shows the SST-W4 pattern in the observed (Fig. 1a) and simulated (Fig. 1g) over the subtropical-midlatitude Southern Hemisphere. The model performs well in reproducing this pattern, exhibiting a high pattern correlation of 0.63 at 0.5°×0.5° spatial resolution with that of observation (significant at a 99% confidence interval, de-correlation spatial scale ~20°×20°). However, subtle differences are noticeable in the pattern over eastern New Zealand, southern Australia, and the eastern Indian Ocean. The second mode explains 6.8% (8.1%) of the total variances in the simulated (observed) data for the analysis period and are well separated from the 1st and 3rd EOF modes (North et al., 1982) as in the observation. The time series of the second EOF mode (PC-2) for simulated SST is independent of ENSO, the IOD, and the SASD, possessing an insignificant correlation coefficient of -0.07, -0.00, and 0.09, respectively, with their indices. The weak relationship with these climate modes is also found in the observational study by Senapati, Dash, et al., (2021). It should be mentioned that the first EOF mode (variance=9.68%) captures the Subtropical Dipole modes in the South Atlantic and Indian Oceans, having a correlation coefficient of 0.54 and 0.42 with the SASD and the IOSD indices, respectively. It agrees with the results of Morioka et al. (2011, 2012, 2014a). Also, the overlapping of the SST-W4 pattern in the Indian Ocean, as noticed by Senapati et al. (2021a), might lead to a low correlation of 0.33 with the IOSD index. The spatial map of the SST anomaly associated with the IOSD, SASD (Fauchereau et al., 2003; Senapati, Dash, et al., 2021), and SPSD indices are different from the SST-W4 pattern (Fig. S1). Note the covariabilty of IOSD and SASD is evident, in agreement with Fauchereau et al. (2003).

The seasonal dependence of the SST-W4 pattern is further examined by calculating the normalized monthly standard deviation of PC-2 (Figs. 1b, h). The variability of the SST-W4 pattern from December to April is greater than one (Fig. 1h), indicating a seasonal phase locking in the simulated results, consistent with observations (Fig. 1b), although there is a slight difference in the amplitudes. This discrepancy may be attributed to variations in the length of the analysis periods, different mean state, and variability between the observation and the model simulation. We then defined the SST-W4 events as years when the normalized PC-2 exceeds one or minus one standard deviation during austral summer. This criteria resulted in eight positive years (1989-90, 1991-92, 1996-97, 1999-2000, 2004-05, 2006-07, 2010-11, and 2011-12) and six negative years (1979-80, 1984-85, 1986-87, 1987-88, 1997-98, and 2017-18) in the observation. Similarly, we identified 48 positive and 44 negative years in the simulated outputs. Subsequently, we conducted a composite analysis of seasonal SST anomalies during positive SST-W4 events in both the observation data (Figs. 1c-f) and simulation outputs (Figs. 1i-l). The observation reveals that SST anomalies in the subtropics start to appear in the austral spring (September-November), reach their peak in austral summer (December-February), and then gradually decline (Figs. 1c-f). The simulation successfully captures this evolution (Figs. 1i-l). These results validate the model's capability to reproduce the SST-W4 pattern in the subtropical-midlatitude and provides a foundation for investigating the detailed mechanisms underlying the SST-W4 pattern.

3.2 Growth and decay mechanisms of the SST-W4 pattern

In this section, we diagnose the air-sea interaction processes on the growth and decay of the SST-W4 pattern using the CTL simulation results. To do this, we performed a mixed layer heat budget analysis using Eq. (3) at each grid to determine the processes on the tendency of the mixed layer temperature. Since the PC-2 could not be useful to quantify each term in Eq. (3), we define an index for the SST-W4 pattern (W4 index) as follows,

$$[Var]\ W4\ index = [Var]_A + [Var]_C + [Var]_E + [Var]_G - [Var]_B - [Var]_D - [Var]_F - [Var]_H \quad (8),$$

where $[Var]_i$ is defined as the area-averaged anomaly for each variable ($[Var]$) over the box " i=A to H" (black boxes in Fig. 2a). The index represents the difference in area-averaged anomaly of positive and negative poles over the boxes. The selection of the boxes is based on the significant SST anomaly regions seen in composite years (Fig. 2a). It should be noted that the overall results are not sensitive to variation in the area of the boxes within the anomalous region. Each pole (Fig. 2a) in the SST-W4 pattern peaks during austral summer in both positive (Fig. 2b) and negative (Fig. 2c) years. The defined SST-W4 index shows a very high significant correlation, 0.88 (0.85), between the PC-2 time series of the simulated (observed) data. Note that the regions selected for both simulated and observed analysis are the same. The composite map generated using the SST-W4 index for positive and negative years matches well with that produced using the PC-2 time series. Further, the budget of each pole for both positive and negative years are similar with opposite signs (Fig. S2). Hence, the index is robust for further analysis. Hereafter, the W4 index is used with other variables to quantify terms in understanding the physical processes involving the air-sea interaction.

3.2.1 Growth Phase

The growth phase of the SST-W4 pattern is investigated by calculating the MLT (T_m) tendency using Eq. (3) for positive (Fig. 3a) and negative (Fig. S3a) composite years. During both the positive and negative years, the MLT anomaly grows from October to January and decays afterward. Since the processes are mirror images for the positive and negative years (Figs. 3, S3), here we discuss the mechanism for the positive years only. The growth (decay) phase refers to the positive (negative) MLT tendency in positive years. The growth (decay) is dominated by the anomalous net surface heat flux (entrainment) term (Fig. 3a). Here, the role of the horizontal advection term is negligible for the growth and decay of the SST-W4 pattern. With the increase in net surface heat flux term, the MLT begins to increase from October, although the contribution from residual terms remains consistently negative. However, after January, NSHF term begins to decrease, and entrainment term dominates (Fig. 3a). As a result, the MLT begins to decrease, and eventually decays. To gain a deeper understanding of the dynamics, we decomposed the net surface heat flux term into four components (i.e., NSW, NLW, LHF, SHF), as illustrated in Fig. 3b. We find the dominant role of anomalous shortwave radiation in the net surface heat flux term. Though anomalous LHF opposes the growth of the SST-W4 pattern (Fig. 3b), the anomalous shortwave radiation generates the SST-W4 pattern. To further dig into the physical mechanism, the contribution of surface heat fluxes during the interannual variation in Eq. (3) is decomposed as

$$\delta\left(\frac{Q_{net}-q_d}{\rho c_p H}\right)\left[\equiv \delta\left(\frac{Q}{\rho c_p H}\right)\right] = \frac{\delta Q}{\rho c_p \overline{H}} - \frac{\delta H \overline{Q}}{\rho c_p \overline{H}^2} + Res. \qquad (9),$$

where overbar and $\delta(\,)$ represent the climatology and their monthly anomaly, respectively. Different terms in the right hand side of Eq. (9) represents (i) the contribution of the surface heat flux anomalies (δQ) acting on a climatological MLD ($\overline{H}$), (ii) the contribution of the MLD anomalies (δH) under climatological heating/cooling ($\overline{Q}$), and (iii) residual terms. The contribution of each term in Eq. (9) for anomalous shortwave radiation and LHF is computed and shown in Figs. 3c,d. The second term in Eq. (9) plays a significant role in the anomalous contribution of the shortwave radiation (Fig. 3c). It means that the warming of the mixed layer is enhanced (suppressed) by the climatological shortwave radiation (Figs. 3c,f) with the thinner (thicker) MLD (Fig. 3e). On the other hand, the LHF is always negative, and the cooling (warming) of the MLT is enhanced by the thinner (thicker) mixed layer (Fig. 3d). However, the decreased (increased) LHF enhances the warming (cooling) as suggested in Fig. 3f, offsets the effect of MLT cooling (warming) by the thinner (thicker) mixed layer (Fig. 3d). The notable residual term, characterized by its significant influence, prevents the growth of the MLT (Fig. 3a). This term encompasses oceanic diffusion and other high-frequency variability.

The interannual MLD anomaly may be linked to the surface heat flux and wind stirring anomalies. To explore the relative contributions, we calculated H_{MO} anomaly and the contribution of each term using Eq. (7) during several seasons for both positive (Table 1) and negative years (Table S1). During positive years, H_{MO} anomaly increases from September-November to November-January, then gradually decreases (Table 1), similar to the MLD anomaly (Fig. 3e). With similar temporal evolution and significant months of the MLD anomaly, H_{MO} anomaly successfully captures the dynamics of MLD variability and hence considered for analysis. The interannual variability of H_{MO} is mainly due to the buoyancy term caused by the surface heat flux anomalies (Table 1) in which the LHF anomaly plays a crucial role (Fig. 3f). The role of wind stirring anomaly in the H_{MO} variability is found to be negligible. Thus, the positive LHF (Fig. 3f) causes positive buoyancy (Table 1) in the ocean surface resulting in shallowing of the mixed layer (Fig. 3e) during positive years. In a similar manner, this dynamic behavior is opposite during the negative years (Table S1, Fig. S3).

Hence, anomalies in the mixed layer depth are primarily caused by buoyancy at the ocean's surface, which is mostly driven by the LHF. The interaction between incoming climatological solar energy and the mixed layer's thickness, therefore, leads to surface warming or cooling, subsequently aid in the formation of the SST-W4 pattern during the austral summer.

3.2.2 Decay Phase

After reaching its peak during December-January, the MLT anomaly starts decaying for positive and negative years mainly due to entrainment term (Figs. 3a, S3a). During early autumn, the entrainment term plays an essential role in the negative tendency of the MLT anomaly during positive years (Fig. 3a). Whereas, both entrainment and surface heat flux attributed to latent heat terms, are vital during late autumn (Figs. 3a,b,f). It is obvious that decrease in the NSHF will decrease the MLT. However the role of entrainment is not straightforward. To understand the cause of entrainment, the entrainment term in Eq. (3) is decomposed into anomalous contributions of four terms using the following equation,

$$-\delta\left(\frac{\Delta T}{H}w_e\right) = -\frac{\delta(\Delta T)\overline{w_e}}{\overline{H}} - \frac{\delta(w_e)\overline{\Delta T}}{\overline{H}} + \frac{\delta H\overline{\Delta T w_e}}{\overline{H}^2} + Res. \qquad (10).$$

In this context, the first term on the right-hand side of Eq. (10) corresponds to the impact of anomalous ΔT (as described in the methods section) under climatological entrainment velocity and the MLD on the variability of entrainment process. Likewise, the second term signifies the influence of anomalous entrainment velocity with climatological ΔT and MLD on entrainment variability. The third term, in the presence of climatological ΔT and entrainment velocity, accounts for the effect of MLD changes on the entrainment process.

Fig. 4 displays each term of Eq. (10) for both positive and negative years. It is evident that the primary driver of entrainment responsible for the decay of the pattern predominantly stems from the first term in Eq. (10). The first term of Eq. (10) means that the variation in entrainment is due to the changes in the difference in temperature of entrained water (i.e., thermocline) and the mixed layer (Fig. 4). This temperature difference is largely attributed to the MLT anomaly because the change in temperature of entrained water is usually minor (Morioka et al., 2011, 2012; Morioka, Ratnam, et al., 2013). During late autumn, the anomalous contribution of surface heat flux is mostly by the LHF (Figs. 3b,f). Fig. 3d represents the composite time series of anomalous terms in Eq. (9) corresponding to LHF. The LHF anomaly in the late autumn is mostly explained by the contribution of the MLD anomalies (δH) under climatological heating/cooling (i.e. the second term in eq. (9)). The first term plays a minor role in the LHF anomaly in May. Thus, the decay of the MLT anomaly by the climatological LHF is intensified (weakened) by the thinner (thicker) mixed layer during the positive (negative) years, as noticed in Fig. 3e (Fig. S3e). It can be summarised from the analysis of different terms in Eqs. (9) and (10) that the positive (negative) entrainment and the thickening (shallowing) of the mixed layer, decays the MLT in the negative (positive) years, even though the climatological flux remains unchanged. During the decay period, shortwave radiation term still contributes and maintains the SST-W4 pattern (Figs. 3b, S3b) in early autumn, though the LHF term does not contribute much. The influence of shortwave radiation term in early autumn (i.e., positive tendency) may be responsible for the 2-month lag between the entrainment and LHF terms in the decay of the SST-W4 pattern.

To summarize, we have identified that LHF anomaly plays a pivotal role in positive buoyancy at the ocean surface, resisting mixing and thus causing a shallowing of the mixed layer depth. The interaction between incoming climatological solar radiation and the mixed layer's thickness results in surface warming (or cooling) and, consequently, positive (or negative) SST anomalies, which contribute to the development of the SST-W4 pattern during austral summer. Subsequently, the decay of the SST-W4 pattern during austral autumn is attributed to anomalous entrainment caused by the changes in temperature difference between the mixed layer and the water below it, as well as anomalous LHF. This underscores the critical importance of the upper ocean variability in both the growth and decay phases of the pattern. Now the question arises: How does the atmospheric W4 play a role in development of the SST-W4 pattern? The origins of the LHF anomaly linking the SST with atmosphere are elucidated in the subsequent section.

3.3 Linkage of SST-W4 pattern with atmosphere in the subtropical-midlatitude Southern Hemisphere

Following Senapati et al. (2021a), the MCA (see methods for details) is performed among various atmospheric and oceanic variables simulated by the SINTEX-F2 to examine and analyze the generation mechanism of the SST-W4 pattern linked with the atmospheric variability. The SST-W4 pattern emerges as the second mode of the SST anomaly with the meridional wind (V; variance= 13.43%), LHF (variance= 6.71%), and MLD (variance=8.42%) anomalies (Figs. 5a-c). It shoud be noted that, the role of zonal wind anomaly in the development of zonal SST pattern throughout the region is negligible (Fig. 5a) and hence omitted in this study. The SST pattern in the MCA (shaded; Fig. 5a) is similar to the earlier result of the second EOF mode (Fig. 1g). A strong correlation (0.85) is found between the expansion coefficient of SST pattern of second MCA mode and EOF method. The net surface heat flux anomaly is mostly dominated by the LHF anomaly compared to other surface fluxes in the generation of the SST-W4 pattern (Figs. S4, 3f) and hence considered here. Note that, all the 2nd modes obtained from the MCA are significantly independent from other modes (Table S2).

The difference in the centre of action between the SST and V is noticeable (Fig. 5a) and can be explained by their interactions with the MLD (Fig. 5b) and LHF (Fig. 5c) (Senapati, Dash, et al., 2021). Figs. 5d and 5e show the auto-correlation and cross-correlation of the variables to examine the evolution of the SST-W4 mode. The auto-correlation of the SST, MLD, V, and LHF indicates their persistence up to 7, 4, 1, and 1 month respectively (Fig. 5d). Cross-correlations of SST-MLD, SST-V, and MLD-V bring out the origin of SST and MLD signals in response to the meridional wind. On the other hand, the LHF shows a significant link with the V (correlation coefficient of 0.4). Interestingly, the MLD, V, and LHF covary with no lag. The SST also exhibits maximum association with V at a one-month lag. Thus, cross-correlation analysis suggests that the meridional wind forces the ocean surface to generate the SST-W4 signal via MLD and LHF. The fading of atmospheric signals when the SST takes the lead is also noticeable (Fig. 2e). Nevertheless, the MLD significantly persists up to 4 months after SST takes a lead, which helps the SST-W4 pattern to remain for a while. The transfer of heat from the ocean to the atmosphere after the SST peak reverses the flux pattern and their cross-correlations after one month (Fig. 2e). The meridional wind could transport warm moist air (cool dry air) from tropical (polar) region to mid-latitude causing the humidity difference in the air-sea interface, and resulting in the LHF varibilty (Senapati, Dash, et al., 2021).

The spatial correlation of PC-2 with meridional wind anomalies (shaded) and geopotential height anomalies (contours) at 250, 500, and 850 hPa depicts an equivalent barotropic structure of the W4 pattern in the troposphere (Fig. S5). The source and dynamics of the atmospheric wave that generates a similar pattern in the SST are investigated by using composite analysis (Fig. 6) and RWS analysis (Fig. 7). Fig. 6 shows the monthly composite maps of horizontal wind and geopotential height anomalies at 250 hPa for the months before the SST-W4 events (Figs. 6a–d). In September, three cells of geopotential height and wind anomalies are positioned in the South Pacific. One cell with a negative geopotential height is located over south of New Zealand. The other two cells are found with dipole-like structures oriented in a north-south direction in the eastern Pacific (Fig. 6a). A prominent cell of positive anomaly is also seen over the south of the African continent (Fig. 6a).

In October, the negative (positive) SST anomaly (Fig. 6e) over the western and eastern (central) South Pacific suppresses (enhances) the convective activity as represented by anomalous precipitation and Outgoing Longwave Radiation (OLR) (shading and contours; Fig. 6f) and hence the accompanied positive (negative) velocity potential anomaly (contours; Fig. 6e) and upper-level convergence (divergence) (vectors; Fig. 6e). As a result, the negative geopotential height anomaly strengthens and expands over the off-shore of New Zealand (Fig. 6b). At the same time, the negative geopotential height moves further southeast in the eastern South Pacific (Fig. 6b). Also, a positive geopotential height anomaly in east Australia and the western Pacific is noticeable (Fig. 6b). In the following months, a well-developed atmospheric W4 pattern appears in the subtropical-midlatitide Southern Hemisphere (Figs. 6c-d). It is mainly due to the Rossby wave train emanating from the SWSP and confined in the westerly jet (solid blue contours in Fig. 6), as evident from the WAF (vectors; Fig. 6f).

This scenario is a mirror image during negative years (Figs. 6g-l). Climatologically, the precipitation band in 60°S-40°S (Fig. S6a) mainly corresponds to the relatively warm mean SST (Fig. S6b) and the strong meridional SST gradient. The region is also influenced by atmospheric circulations that promote moisture transport to the region from the tropical region. The SST anomaly over the SWSP with a climatological SST of around 25°C in 40°S-30°S (Fig. S6b) triggers the convective activity (as seen in OLR) and causes anomalous rainfall over there (Figs. 6e,f,k,l). Positive (negative) precipitation, negative (positive) OLR, negative (positive) velocity potential and divergence (convergence) during negative (positive) years suggest a diabatic source (sink) over the SWSP (Figs. 6e,f,k,l). However, the co-occurrence of precipitation, OLR, and velocity potential anomalies in other regions like the South Atlantic and central and eastern South Pacific creates an ambiguity regarding the possible sources that trigger the atmospheric W4 pattern. The RWS is calculated using Eq. (1), which consists mainly of the stretching of the vortex by eddies (Term-1) and the advection of absolute vorticity by divergent wind (Term-2). Since the peak of the SST-W4 pattern occurs with a 2-month lag of convective activity (i.e., October-November; Fig. 6), a correlation map is constructed between PC-2 of austral summer and anomalous RWS (Fig. 7a), Term-1 (Fig. 7b), and Term-2 (Fig. 7c) during October-November. The anomalous RWS shows three prominent areas in the subtropical Pacific (Fig. 7a) due mainly to the anomaly in Term-1 (Fig. 7b) as the possible source of the atmospheric W4 pattern. The contribution of anomalous Term-2 in RWS anomaly is negligible (Fig. 7c). Basically, Term-1 anomaly includes the anomalous RWS activity due to anomalous divergence under climatological absolute vorticity and hence the atmospheric W4 pattern. Since the Rossby wave travels eastward guided by the westerly jet in the Southern Hemisphere, the upstream region in the SWSP is a potential source for the atmospheric W4 pattern. The WAF anomaly emitted from the SWSP (vectors, Figs. 6f,l) corresponding to precipitation-induced diabatic heating/cooling (shaded, Figs. 6f,l), OLR anomalies (contours, Figs. 6f,l), velocity potential anomaly (contours; Figs. 6e,k), and anomalous divergence (vectors, Figs. 6e,k) validates the RWS over the SWSP as the probable source in generating the atmospheric W4 pattern. Here, a natural question arises: What favors the formation of atmospheric W4 Rossby waves?

To identify such factors, we investigated the properties of the background atmospheric flow in the propagation of the Rossby wave during the development of the atmospheric W4 pattern. The stationary Rossby wavenumber K_s [$=(\beta_M/\overline{u})^{1/2}$] is estimated for this purpose; where $\overline{u}$ denote the mean zonal wind. Here, β_M ($=\beta-\overline{u}_{yy}$) comprising β and $\overline{u}_{yy}$ represents the meridional gradient of planetary vorticity and the time mean of the meridional relative vorticity gradient, respectively (B. J. Hoskins & Ambrizzi, 1993). Fig. 8 shows the K_s and its components during the November-January months for the positive (left panel, Fig. 8) and negative (right panel, Fig. 8) SST-W4 years. The existence of the stationary W4 in the midlatitude between 30°S to 60°S is clearly evident during both positive and negative SST-W4 years (red contour, Fig. 8a). This is due to the effective meridional gradient in planetary vorticity (Fig. 8b) guided by the curvature of the westerly jet (Fig. 8c). Therefore, the climatological background flow (during November-January) is necessary to establish the disturbance over the SWSP into an atmospheric wavenumber-4 pattern in the Southern Hemisphere.

3.4 Potential source of the SST and atmospheric W4 patterns

The above intriguing results indicate the role of the SWSP in generating the SST and atmospheric W4 patterns. To examine the root cause of the convective activity over the SWSP and its role in developing the SST and atmospheric W4 patterns, we conducted sensitivity experiments with the SINTEX-F2 (see Section 2.2). Prior to conducting any sensitivity experiments, it is imperative to acknowledge that the SINTEX-F2 demonstrates a high level of skill in capturing and predicting tropical and subtropical climate dynamics and their teleconnections up to seasonal scales (Doi et al., 2016). Therefore, the analysis of sensitivity experiments involving the nudging of the tropical and SWSP towards climatological value (noTropics and noSWSP) in the SINTEX-F2 is considered robust. The selection of the noSWSP sensitivity experiment area is based on the potential RWS (Fig. 7a), precipitation and OLR patterns (Figs. 6f,l), and velocity potential and divergence patterns (Figs. 6e,k) associated with the SST and atmospheric W4 patterns. The spatial patterns of the second EOF mode of SST anomaly for all the simulations are shown in Fig. 9. It shows the SST-W4 pattern in the second mode for early 70 yr of CTL simulation (Fig. 9a), which shows similar features as of Fig. 1g. In the noTropics, the SST over the tropical region (25°S-25°N) is nudged to the climatological SST to suppress the influence of tropical region on the SWSP climate variability (Liess et al., 2014), so also on the generation of the W4 patterns. Interestingly, the EOF pattern remains unchanged (Fig. 9b), suggesting the generation mechanisms are not dependent on the variations of the SST in the tropical regions. Therefore, it can be hypothesized that the variability over the SWSP might be locally generated or influenced by the polar regions. To confirm this, we perform the noSWSP experiment by nudging the SST to its climatological value over the SWSP (black rectangle box, Fig. 9c). In the absence of air-sea interaction due to the SST anomalies over the SWSP supresses the SST and atmospheric W4 patterns in the southern subtropics-midlatitudes (Fig. 9c), especially over the Indian Ocean and the ocean to south of Australia. The SST anomalies over the eastern Pacific and Atlantic Oceans are not sensitive to the SWSP SST variability, as seen in the Fig. 9c. Thus, the local air-sea interaction over the SWSP is crucial for the generation of the SST and atmospheric W4 patterns.

The composite analysis of CTL, noTropics, and noSWSP simulation further provides an insight to the dynamical mechanisms involved. The left panel in Fig. 10 shows the SST anomaly (shaded) and 850 hPa wind anomaly (vectors) for positive composite years in the CTL, noTropics, and noSWSP simulations (Figs. 10a-c). Same for the negative years are shown in Figs. S7a-c. Similarly, the middle and right panels show the geopotential height anomalies (shaded) and WAF (vectors) at 250 hPa (Figs. 10d-f), and precipitation (shaded) and divergent wind anomalies (vectors) at 250 hPa (Figs. 10g-i), respectively. During positive years in the CTL simulation, wave activity flux emanating from the SWSP (vectors; Fig. 10d) in response to precipitation (i.e., diabatic heating) (shaded; Fig. 10g) and divergent wind (vectors; Fig. 10g) contributes to the development of the W4 patterns in the 250 hPa geopotential height (shaded; Fig. 10d), 850 hPa wind (vectors; Fig. 10a), and SST (shaded; Fig. 10a) anomalies. The Rossby wave train originates from the SWSP, travels towards Antarctica, where it gets trapped within the nearby westerly jet, subsequently following the great circle path to establish the atmospheric W4 structure in the mid-latitudes (Figs. 10d, g). In the noTropics experiment, the dynamics seen to be similar (Figs. 10b,e,h) with the CTL simulation. The amplitude of SST variances do not change largely in noTropics as compared to CTL simulation (Figs. 9-10). Similar with atmospheric variables as well (Figs. 10e, h). Also, the frequency of occurrence (i.e., 19 extreme years in both CTL and noTropics) remains the same, suggesting the weak relation of the W4 pattern with the tropics. In fact, the Subtropical Dipoles in each basin can be generated owing to the SAM in the absence of tropical climate variability (Morioka et al., 2014a). However, in the W4 case, the geopotential height does not vary over mid and high latitudes in the noTropics experiment, omitting the role of the SAM in SST and atmospheric W4 patterns (Fig. 10e). In addition, the convective activity over the SWSP is unaffected from the tropical region (Fig. 10h). Recently, the role of SAM is also found to be negligible in generation of zonal wavenumber-3 in absence of perturbation in tropics or subtropics (Goyal et al., 2021). Thus, it can be concluded that, the generation mechanisms of SST and atmospheric W4 patterns are not affected by the tropical climate.

Conversely, in the reduction of convective activity over the SWSP, as demonstrated in the noSWSP experiment (Fig. 9c), both the circumglobal SST and atmospheric W4 patterns dissipate. The rainfall deficit amounts to -18.3, -13.1, and -7.3 mm month^{-1} in the CTL, noTropics, and noSWSP experiments during positive years, respectively. This significant decrease in convection activity in the noSWSP experiment compared to the CTL experiment, implies much differences in the generation dynamics between the experiments (Figs. 10c, f, i). Due to less convective activity in the SWSP region, the Rossby wave train fails to propagate circumglobally and cannot form the characteristic W4 atmospheric structure. In this scenario, the Rossby waves emanating from the southeast of SWSP become trapped within a waveguide, propagating toward the equator over South America, not reaching the South Atlantic. As a consequence, the W4 pattern in SST and atmosphere could not be establish in the subtropical-midlatitude Southern Hemisphere. The scenario is the opposite during negative years (Fig. S7). It is interesting to observe the negative SAM in noSWSP experiment during positive years (Fig. 10f). It could be due to the overwhelming role of the SAM, the dominant atmospheric intrinsic variability in the Southern Hemisphere, where the W4 patterns linked to SWSP are superposed. The SST anomalies, specifically over south Atlantic and Indian Ocean seems to be related to the negative SAM in noSWSP experiment (Ciasto & Thompson, 2008; Screen et al., 2010).

Despite convective activity in other regions in the noSWSP experiment, SST and atmospheric W4 pattern generation is absent, confirming the essential role of SWSP in this process. Hence the noSWSP experiment concludes that variability in the SWSP as a necessary condition for forming the circumglobal Rossby waves and, subsequently, the SST and atmospheric W4 patterns. The behavioral change in the Rossby wave propagation without the SST anomalies over the SWSP requires further investigation in future studies.

4 Summary and Discussion

Using the SINTEX-F2, we have demonstrated the W4 pattern of SST anomalies in the subtropical-midlatitude Southern Hemisphere. A realistic simulation of the W4 pattern in the CGCM has allowed us to conduct a comprehensive investigation of the generation mechanisms using the model experiments. The results are summarized using a schematic diagram (Fig. 11). (1) The convection activities and associated divergent wind anomaly over the SWSP stretch the vortex near the westerly jet due to diabatic heating and divergent wind during October-November. (2) This disturbance gets trapped in the westerly waveguide and circumnavigates the globe, establishing an atmospheric W4 pattern over the southern midlatitudes. The disturbance follows the meridional gradient of effective planetary vorticity and is guided by the curvature of the mean zonal flow, forming an atmospheric W4 pattern. The atmospheric W4 pattern has an equivalent barotropic structure in the troposphere and interacts with the upper ocean in the southern subtropics and midlatitudes. The air-sea interaction processes involved in the growth and decay of the SST-W4 pattern are investigated using mixed layer budget analysis. We also defined an index for the SST-W4 pattern to perform the budget analysis. (3, 4) The anomalous wind induces a variation in the MLD via a LHF anomaly over the region. (5) Because incoming climatological solar energy is absorbed in a thinner (thicker) mixed layer, the shallower (deeper) MLD supports surface warming (cooling). (6) In this way, the SST-W4 is generated in the southern subtropics and midlatitudes via a thermodynamic coupling between the upper ocean and atmosphere. Then, the SST-W4 pattern experiences the following three processes and starts decaying during austral autumn. Most dominantly, (7) the entrainment caused by the difference in temperature between the entrained water and the mixed layer causes the SST pattern to disapper in early autumn. The disappearance of the atmospheric wave is also an important cause of the pattern's decay during early autumn. Also, the anomalous LHF, which turns around after SST forcing, induces cooling (warming) over the warm (cold) pole and hence contributes to the decay of the SST-W4 pattern in late autumn.

The SINTEX-F2 has the ability to capture subtropical-midlatitude dynamics on a global scale. Although air-sea interaction processes are similar to those of Subtropical Dipoles in each basin (Morioka et al., 2011, 2012; Morioka, Ratnam, et al., 2013), this study highlights the role of ocean mixed layer in the life cycle of the SST-W4 pattern for the first time. The subsurface warming may have implications for the MLT, yet our investigation reveals no evidence of such warming in our study area, as confirmed by both observational data (Orsi, 1998; Orsi & Whitworth, 2005) and SINTEX-F2 model outputs (Fig. S8).

Of particular interest is the weakening of the WAF over the South Atlantic and Indian Ocean during positive years (Figs. 6a-f). The influence of the SAM during positive years is apparent in the noSWSP experiment (Fig. 10f). SST anomalies, especially those over the South Atlantic and Indian Ocean, appear to correlate with the negative SAM in the noSWSP experiment (Ciasto & Thompson, 2008; Screen et al., 2010). However, the role of the SAM is not evident during positive years in the CTL experiment (Fig. 10d), though it becomes apparent during negative years (Fig. S7d). Thus, while the SAM may contribute to maintaining SST and atmospheric W4 over the South Atlantic and Indian Oceans, further investigation is required for clarification. Additionally, the presence of positive HGT over the southwestern Indian Ocean from September onwards, strengthening in subsequent months, is notable during positive years compared to negative years (Fig. 6). However, the role of the southwestern Indian Ocean in the development of SST and atmospheric W4 falls outside the scope of our study (Figs. 6a-f).

On the other hand, interaction of the SST-W4 pattern with the Subtropical Dipoles, South Atlantic-southern Indian ocean pattern (Lin, 2019), mid-tropospheric semi-permanent anticyclones (C. J. C. Reason, 2016), SAM, Pacific South American patterns (Grimm & Ambrizzi, 2009), subtropical highs are intriguing but leave open questions for future work. Along with this, the contribution of SST-W4 variability apart from the Subtropical Dipoles in modulating rainfall over southern continents directly or by a local response (Morioka et al., 2015) needs further numerical modeling experiments. Furthermore, sensitivity experiments confirm the little involvement of the tropical forcings and SAM in the dynamics of SST and atmospheric W4 patterns, which contrasts with the probable sources of Subtropical Dipoles (Morioka et al., 2014a). In these sensitivity experiments, the precipitation and divergent wind anomalies seen in the SST nudged areas might be due to the high-frequency variabilities. The local air-sea interaction over the SWSP is found to be the necessary condition for the generation of SST and atmospheric W4 patterns. However, it will be interesting to quantify the amount of precipitation/diabatic heating over the SWSP that necessary for the generation of W4 pattern. The role of the tropical climate in the W4 pattern on a decadal timescale (which is related to SPMM; Senapati et al., 2022), and the linkage of the Tasman Sea with tropical regions (Liess et al., 2014) cannot be neglected. In the absence of tropical climate variation, the W4 pattern can be generated but the tropical climate variability may play a role in modulating the W4 pattern through atmospheric teleconnection and changes in local SST over Tasman Sea, which will be studied in the future. The Rossby wave teleconnection from the SWSP in the absence of tropical influence provides new insights into subtropical climate variability. For example, studies suggest that the relationship between ENSO and the Antarctic sea ice has changed in recent decades because of the reduced response of the Tasman Sea to ENSO (Dou & Zhang, 2022). Therefore, a better understanding of the linkage between the Southern Hemisphere climate variability and the SWSP is required.

Acknowledgments

We performed the SINTEX-F2 model experiment on Data Analyzer (DA) system at JAMSTEC. The first author is thankful to the Department of Science and Technology, New Delhi, India, for funding his research through the INSPIRE Ph.D. fellowship programme (IF170092). The first author visited JAMSTEC for six months in support of a bursary from Antarctic Science Ltd, British Antarctic Survey, Natural Environment Research Council, United Kingdom to analyze the SINTEX-F2 results. The authors are also grateful to the Application Laboratory, Japan Agency for Marine-Earth Science and Technology, Japan, the University of Reading, UK, and the Indian Institute of Technology Kharagpur, India, for providing the necessary facilities to perform this research. NCAR Command Language, Climate Data Operator, Python, and Matlab have been used for the analysis. Figures are plotted using PyFerret, Python, and Matlab.

Open Research

The observed SST data (Rayner et al., 2003) is available on the HadISST website (https://www.metoffice.gov.uk/hadobs/hadisst/data/download.html). SINTEX-F2 model output used to make figures in this study will be available from the Zenodo repository by the time of manuscript publication.

References

Anila, S., & Gnanaseelan, C. (2023). Coupled feedback between the tropics and subtropics of the Indian Ocean with emphasis on the coupled interaction between IOD and SIOD. *Global and Planetary Change*, *223*, 104091. https://doi.org/10.1016/j.gloplacha.2023.104091

Ashok, K., Guan, Z., & Yamagata, T. (2003). Influence of the Indian Ocean Dipole on the Australian winter rainfall. *Geophysical Research Letters*. https://doi.org/10.1029/2003GL017926

Barros, V. R., & Silvestri, G. E. (2002). The relation between sea surface temperature at the subtropical south-central Pacific and precipitation in southeastern South America. *Journal of Climate*, *15*(3), 251–267.

Behera, S. K., & Yamagata, T. (2001). Subtropical SST dipole events in the southern Indian Ocean. *Geophysical Research Letters*, *28*(2), 327–330. https://doi.org/10.1029/2000GL011451

Bo Qiu, & Kelly, K. A. (1993). Upper-ocean heat balance in the Kuroshio extension region. *Journal of Physical Oceanography*, *23*(9). https://doi.org/10.1175/1520-0485(1993)023<2027:uohbit>2.0.co;2

Ciasto, L. M., & Thompson, D. W. J. (2008). Observations of Large-Scale Ocean–Atmosphere Interaction in the Southern Hemisphere. *Journal of Climate*, *21*(6), 1244–1259. https://doi.org/10.1175/2007JCLI1809.1

Crétat, J., Terray, P., Masson, S., & Sooraj, K. P. (2018). Intrinsic precursors and timescale of the tropical Indian Ocean Dipole: insights from partially decoupled numerical experiment. *Climate Dynamics*, *51*(4), 1311–1332. https://doi.org/10.1007/s00382-017-3956-7

Davis, R. E., deSzoeke, R., & Niiler, P. (1981). Variability in the upper ocean during MILE. Part II: Modeling the mixed layer response. *Deep Sea Research Part A, Oceanographic Research Papers*, *28*(12). https://doi.org/10.1016/0198-0149(81)90092-3

Diaz, A. F., Studzinski, C. D., & Mechoso, C. R. (1998). Relationships between precipitation anomalies in Uruguay and southern Brazil and sea surface temperature in the Pacific and Atlantic Oceans. *Journal of Climate*, *11*(2), 251–271.

Doi, T., Behera, S. K., & Yamagata, T. (2016). Improved seasonal prediction using the SINTEX-F2 coupled model. *Journal of Advances in Modeling Earth Systems*, *8*(4). https://doi.org/10.1002/2016MS000744

Dong, S., Gille, S. T., & Sprintall, J. (2007). An assessment of the Southern Ocean mixed layer heat budget. *Journal of Climate*, *20*(17). https://doi.org/10.1175/JCLI4259.1

Dou, J., & Zhang, R. (2022). Weakened relationship between ENSO and Antarctic sea ice in recent decades. *Climate Dynamics*, (0123456789). https://doi.org/10.1007/s00382-022-06364-4

Fauchereau, N., Trzaska, S., Richard, Y., Roucou, P., & Camberlin, P. (2003). Sea-surface temperature co-variability in the southern Atlantic and Indian Oceans and its connections with the atmospheric circulation in the Southern Hemisphere. *International Journal of Climatology*, *23*(6), 663–677. https://doi.org/10.1002/joc.905

Fichefet, T., & Maqueda, M. A. M. (1997). Sensitivity of a global sea ice model to the treatment of ice thermodynamics and dynamics. *Journal of Geophysical Research: Oceans*, *102*(C6). https://doi.org/10.1029/97JC00480

Goyal, R., Jucker, M., Sen Gupta, A., Hendon, H. H., & England, M. H. (2021). Zonal wave 3 pattern in the Southern Hemisphere generated by tropical convection. *Nature Geoscience*, *14*(10), 732–738. https://doi.org/10.1038/s41561-021-00811-3

Grimm, A. M., & Ambrizzi, T. (2009). Teleconnections into South America from the Tropics and Extratropics on Interannual and Intraseasonal Timescales. https://doi.org/10.1007/978-90-481-2672-9_7

Grimm, A. M., Barros, V. R., & Doyle, M. E. (2000). Climate variability in southern South America associated with El Nino and La Nina events. *Journal of Climate*, *13*(1). https://doi.org/10.1175/1520-0442(2000)013<0035:CVISSA>2.0.CO;2

Hermes, J. C., & Reason, C. J. C. (2005). Ocean model diagnosis of interannual coevolving SST variability in the South Indian and South Atlantic Oceans. *Journal of Climate*. https://doi.org/10.1175/JCLI3422.1

Hoskins, B. J., & Ambrizzi, T. (1993). Rossby wave propagation on a realistic longitudinally varying flow. *Journal of the Atmospheric Sciences*. https://doi.org/10.1175/1520-0469(1993)050<1661:RWPOAR>2.0.CO;2

Hoskins, Brian J, & Karoly, D. J. (1981). The steady linear response of a spherical atmosphere to thermal and orographic forcing. *Journal of the Atmospheric Sciences*, *38*(6), 1179–1196.

Jianchun Qin, & Robinson, W. A. (1993). On the Rossby wave source and the steady linear response to tropical forcing. *Journal of the Atmospheric Sciences*. https://doi.org/10.1175/1520-0469(1993)050<1819:otrwsa>2.0.co;2

Kraus, E. B., & Turner, J. S. (1967). A one-dimensional model of the seasonal thermocline II. The general theory and its consequences. *Tellus*, *19*(1). https://doi.org/10.3402/tellusa.v19i1.9753

Larson, S. M., Pegion, K. V., & Kirtman, B. P. (2018). The South Pacific meridional mode as a thermally driven source of ENSO amplitude modulation and uncertainty. *Journal of Climate*, *31*(13), 5127–5145.

Liess, S., Kumar, A., Snyder, P. K., Kawale, J., Steinhaeuser, K., Semazzi, F. H. M., et al. (2014). Different modes of variability over the Tasman Sea: Implications for regional climate. *Journal of Climate*, *27*(22). https://doi.org/10.1175/JCLI-D-13-00713.1

Lin, Z. (2019). The South Atlantic-South Indian ocean pattern: A zonally oriented teleconnection along the Southern Hemisphere westerly jet in austral summer. *Atmosphere*, *10*(5). https://doi.org/10.3390/atmos10050259

Liu, Z., & Alexander, M. (2007). Atmospheric bridge, oceanic tunnel, and global climatic teleconnections. *Reviews of Geophysics*. https://doi.org/10.1029/2005RG000172

Luo, J. J., Masson, S., Roeckner, E., Madec, G., & Yamagata, T. (2005). Reducing climatology bias in an ocean-atmosphere CGCM with improved coupling physics. *Journal of Climate*, *18*(13). https://doi.org/10.1175/JCLI3404.1

Madec, G. (2008). NEMO ocean engine: Note du pole de modélisation, Institut Pierre-Simon Laplace (IPSL), France, No 27 ISSN No 1288-1619. *Technical ReportTech. Rep*.

Madec, Gurvan, & Imbard, M. (1996). A global ocean mesh to overcome the North Pole singularity. *Climate Dynamics*, *12*(6). https://doi.org/10.1007/BF00211684

Madec, Gurvan, Delecluse, P., Imbard, M., & Levy, C. (1998). OPA 8.1 Ocean General Circulation Model Reference Manual. *Notes Du Pôle de Modélisation, Institut Pierre Simon Laplace*. https://doi.org/10.2478/adms

Masson, S., Terray, P., Madec, G., Luo, J. J., Yamagata, T., & Takahashi, K. (2012). Impact of intra-daily SST variability on ENSO characteristics in a coupled model. *Climate Dynamics*, *39*(3). https://doi.org/10.1007/s00382-011-1247-2

Merryfield, W. J., Holloway, G., & Gargett, A. E. (1999). A global ocean model with double-diffusive mixing. *Journal of Physical Oceanography*, *29*(6). https://doi.org/10.1175/1520-0485(1999)029<1124:AGOMWD>2.0.CO;2

Mo, K. C., & Paegle, J. N. (2001). The Pacific-South American modes and their downstream effects. *International Journal of Climatology*, *21*(10). https://doi.org/10.1002/joc.685

Morioka, Y., & Behera, S. K. (2021). Remote and Local Processes Controlling Decadal Sea Ice Variability in the Weddell Sea. *Journal of Geophysical Research: Oceans*, *126*(8), e2020JC017036. https://doi.org/10.1029/2020JC017036

Morioka, Y., Tozuka, T., & Yamagata, T. (2011). On the growth and decay of the subtropical dipole mode in the South Atlantic. *Journal of Climate*. https://doi.org/10.1175/2011JCLI4010.1

Morioka, Y., Tozuka, T., Masson, S., Terray, P., Luo, J. J., & Yamagata, T. (2012). Subtropical dipole modes simulated in a coupled general circulation model. *Journal of Climate*, *25*(12), 4029–4047. https://doi.org/10.1175/JCLI-D-11-00396.1

Morioka, Y., Ratnam, J. V., Sasaki, W., & Masumoto, Y. (2013). Generation mechanism of the South Pacific subtropical dipole. *Journal of Climate*. https://doi.org/10.1175/JCLI-D-12-00648.1

Morioka, Y., Tozuka, T., & Yamagata, T. (2013). How is the Indian Ocean Subtropical Dipole excited? *Climate Dynamics*, *41*(7–8), 1955–1968. https://doi.org/10.1007/s00382-012-1584-9

Morioka, Y., Masson, S., Terray, P., Prodhomme, C., Behera, S. K., & Masumoto, Y. (2014a). Role of tropical SST variability on the formation of subtropical dipoles. *Journal of Climate*, *27*(12), 4486–4507. https://doi.org/10.1175/JCLI-D-13-00506.1

Morioka, Y., Masson, S., Terray, P., Prodhomme, C., Behera, S. K., & Masumoto, Y. (2014b). Role of tropical SST variability on the formation of subtropical dipoles. *Journal of Climate*, *27*(12), 4486–4507. https://doi.org/10.1175/JCLI-D-13-00506.1

Morioka, Y., Takaya, K., Behera, S. K., & Masumoto, Y. (2015). Local SST impacts on the summertime mascarene high variability. *Journal of Climate*, *28*(2), 678–694. https://doi.org/10.1175/JCLI-D-14-00133.1

North, G. R., Bell, T. L., Cahalan, R. F., & Moeng, F. J. (1982). Sampling Errors in the Estimation of Empirical Orthogonal Functions. *Monthly Weather Review*. https://doi.org/10.1175/1520-0493(1982)110<0699:seiteo>2.0.co;2

Orsi, A. H. (1998). WOCE Atlas Volume 1: Southern Ocean Hydrographic Web Atlas. https://doi.org/10.21976/C6BC78

Orsi, A. H., & Whitworth, T. (2005). Hydrographic Atlas of the World Ocean Circulation Experiment (WOCE): Volume 1: Southern Ocean.

Paegle, J. N., & Mo, K. C. (2002). Linkages between summer rainfall variability over South America and sea surface temperature anomalies. *Journal of Climate*, *15*(12), 1389–1407.

Paulson, C. A., & Simpson, J. J. (1977). Irradiance Measurements in the Upper Ocean. *Journal of Physical Oceanography*, *7*(6). https://doi.org/10.1175/1520-0485(1977)007<0952:imituo>2.0.co;2

Rayner, N. A., Parker, D. E., Horton, E. B., Folland, C. K., Alexander, L. V., Rowell, D. P., et al. (2003). Global analyses of sea surface temperature, sea ice, and night marine air temperature since the late nineteenth century [Dataset]. *Journal of Geophysical Research: Atmospheres*. https://doi.org/10.1029/2002jd002670

Reason, C. (1999). Interannual warm and cool events in the subtropical/mid-latitude South Indian Ocean Region. *Geophysical Research Letters*, *26*(2), 215–218.

Reason, C. (2001). Subtropical Indian Ocean SST dipole events and southern African rainfall. *Geophysical Research Letters*, *28*(11), 2225–2227.

Reason, C. J. C. (2016). The Bolivian, Botswana, and Bilybara Highs and Southern Hemisphere drought/floods. *Geophysical Research Letters*, *43*(3), 1280–1286. https://doi.org/10.1002/2015GL067228

Richard, Y., Trzaska, S., Roucou, P., & Rouault, M. (2000). Modification of the southern African rainfall variability/ENSO relationship since the late 1960s. *Climate Dynamics*, *16*(12). https://doi.org/10.1007/s003820000086

Rodrigues, R. R., Campos, E. J. D., & Haarsma, R. (2015). The impact of ENSO on the south Atlantic subtropical dipole mode. *Journal of Climate*, *28*(7). https://doi.org/10.1175/JCLI-D-14-00483.1

Roeckner, E., Bäuml, G., Bonaventura, L., Brokopf, R., Esch, M., Giorgetta, M., et al. (2003). The atmospheric general circulation model ECHAM 5. PART I: Model description. Report / MPI für Meteorologie. http://hdl.handle.net/11858/00-001M-0000-0012-0144-5. *Report / Max-Planck-Institut Für Meteorologie*, (349).

Saji, N. H., Goswami, B. N., Vinayachandran, P. N., & Yamagata, T. (1999). A dipole mode in the tropical Indian ocean. *Nature*. https://doi.org/10.1038/43854

Sardeshmukh, P. D., & Hoskins, B. J. (1988). The generation of global rotational flow by steady idealized tropical divergence. *Journal of the Atmospheric Sciences*. https://doi.org/10.1175/1520-0469(1988)045<1228:TGOGRF>2.0.CO;2

Screen, J. A., Gillett, N. P., Karpechko, A. Y., & Stevens, D. P. (2010). Mixed Layer Temperature Response to the Southern Annular Mode: Mechanisms and Model Representation. *Journal of Climate*, *23*(3), 664–678. https://doi.org/10.1175/2009JCLI2976.1

Senapati, B., Dash, M. K., & Behera, S. K. (2021). Global wave number-4 pattern in the southern subtropical sea surface temperature. *Scientific Reports*, *11*(1), 1–12. https://doi.org/10.1038/s41598-020-80492-x

Senapati, B., Deb, P., Dash, M. K., & Behera, S. K. (2021). Origin and dynamics of global atmospheric wavenumber-4 in the Southern mid-latitude during austral summer. *Climate Dynamics*, *59*(5–6), 1309–1322. https://doi.org/10.1007/s00382-021-06040-z

Senapati, B., Dash, M. K., & Behera, S. K. (2022). Decadal Variability of Southern Subtropical SST Wavenumber-4 Pattern and Its Impact. *Geophysical Research Letters*, *49*(16). https://doi.org/10.1029/2022GL099046

Suzuki, R., Behera, S. K., Iizuka, S., & Yamagata, T. (2004). Indian Ocean subtropical dipole simulated using a coupled general circulation model. *Journal of Geophysical Research C: Oceans*, *109*(9), 1–18. https://doi.org/10.1029/2003JC001974

Takaya, K., & Nakamura, H. (1997). A formulation of a wave-activity flux for stationary Rossby waves on a zonally varying basic flow. *Geophysical Research Letters*, *24*(23). https://doi.org/10.1029/97GL03094

Takaya, K., & Nakamura, H. (2001). A formulation of a phase-independent wave-activity flux for stationary and migratory quasigeostrophic eddies on a zonally varying basic flow. *Journal of the Atmospheric Sciences*. https://doi.org/10.1175/1520-0469(2001)058<0608:AFOAPI>2.0.CO;2

Taschetto, A. S., & Wainer, I. (2008). The impact of the subtropical South Atlantic SST on South American precipitation. In *Annales Geophysicae* (Vol. 26, pp. 3457–3476). Copernicus Publications Göttingen, Germany.

Trenberth, K. E. (1997). The Definition of El Niño. *Bulletin of the American Meteorological Society*, *78*(12). https://doi.org/10.1175/1520-0477(1997)078<2771:TDOENO>2.0.CO;2

Valcke, S. (2006). OASIS3 User Guide (prism_2-5). CERFACS Technical Report TR/CMGC/06/73, PRISM Report No 3, Toulouse, France.

Venegas, S. A., Mysak, L. A., & Straub, D. N. (1997). Atmosphere-ocean coupled variability in the South Atlantic. *Journal of Climate*. https://doi.org/10.1175/1520-0442(1997)010<2904:AOCVIT>2.0.CO;2

Wang, F. (2010). Subtropical dipole mode in the Southern Hemisphere: A global view. *Geophysical Research Letters*, *37*(10), 1–4. https://doi.org/10.1029/2010GL042750

Yasuda, I., Tozuka, T., Noto, M., & Kouketsu, S. (2000). Heat balance and regime shifts of the mixed layer in the Kuroshio Extension. *Progress in Oceanography*. https://doi.org/10.1016/S0079-6611(00)00038-0

You, Y., & Furtado, J. C. (2018). The South Pacific meridional mode and its role in tropical Pacific climate variability. *Journal of Climate*, *31*(24), 10141–10163.

Zhang, H., Clement, A., & Di Nezio, P. (2014). The South Pacific meridional mode: A mechanism for ENSO-like variability. *Journal of Climate*, *27*(2), 769–783.

Figures:

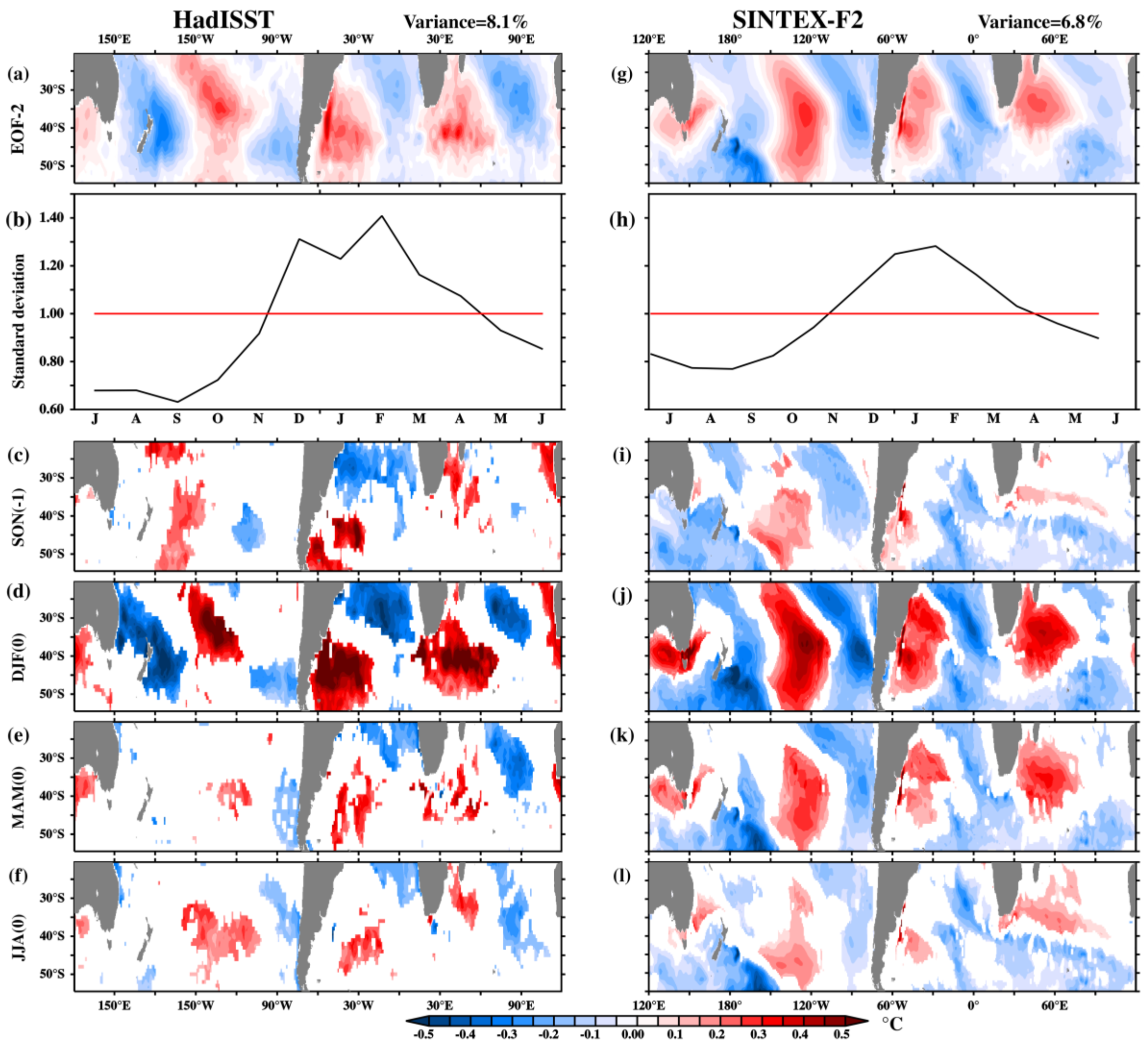

Figure 1. (a) The second EOF mode of SST anomalies (in °C) from HadISST over the subtropical-midlatitude Southern Hemisphere. Values in the top right explain its variance. (b) The normalized monthly standard deviation of the second principal component (PC-2). Composite of the observed SST anomalies (in °C) during (c) SON(-1) (d) DJF(0) (e) MAM(0), and (f) JJA(0) of the positive SST-W4 pattern. "-1 or 0" in the brackets denotes the year before (during) the event year. (c-f) Values exceeding 90% confidence level using a two-tailed Student's *t*-test are colored. (g-l) Same as in (a-f), but for the SINTEX-F2 model results.

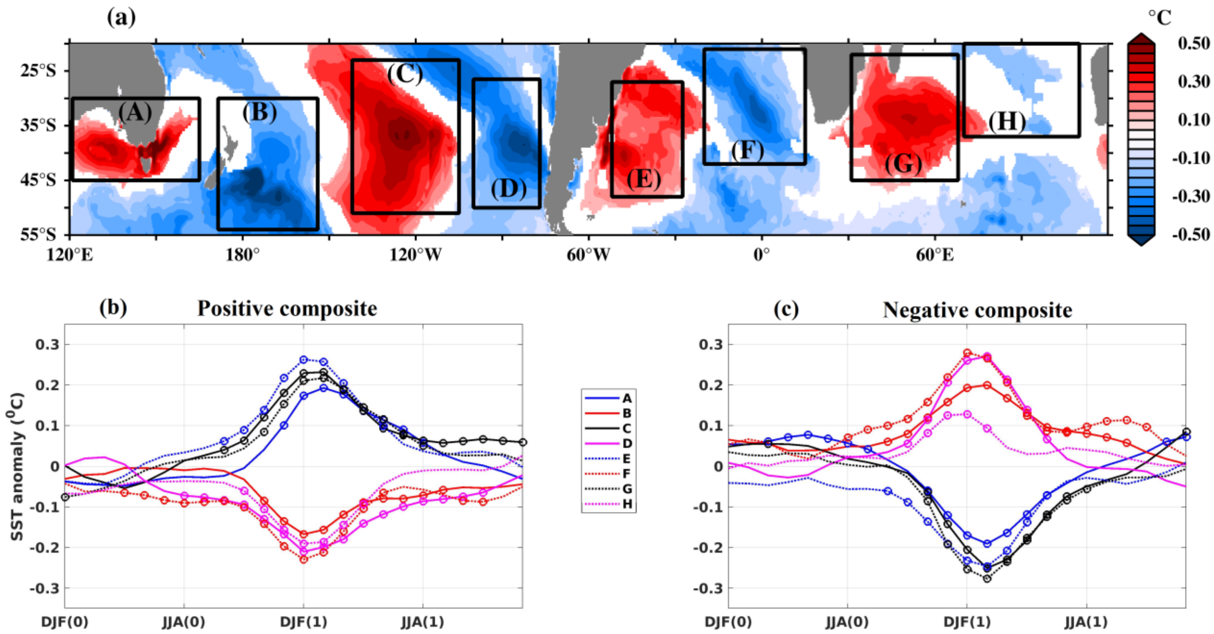

Figure 2. (a) Composite map of SST anomalies (in °C) in the CTL experiment during the austral summer of the positive years. The black rectangular boxes used for calculation of the SST-W4 index correspond to the region A(120°E-165°E, 45°S-30°S), B(170°E-154°W, 55°S-30°S), C(142°W-105°W, 51°S-23°S), D(100°W-77°W, 50°S-26°S), E(52°W-27°W, 48°S-27°S), F(20°W-15°E, 45°S-23°S), G(31°E-68°E, 45°S-22°S), and H(70°E-110°E, 37°S-20°S). (b) Composite time series of SST anomaly averaged over each box during the positive years. (c) Same as in Fig. 2b, but for the negative years. To smooth the time series, a 3-month running mean is applied. Open circles show significant anomalies with 90% confidence levels using a two-tailed Student's *t*-test.

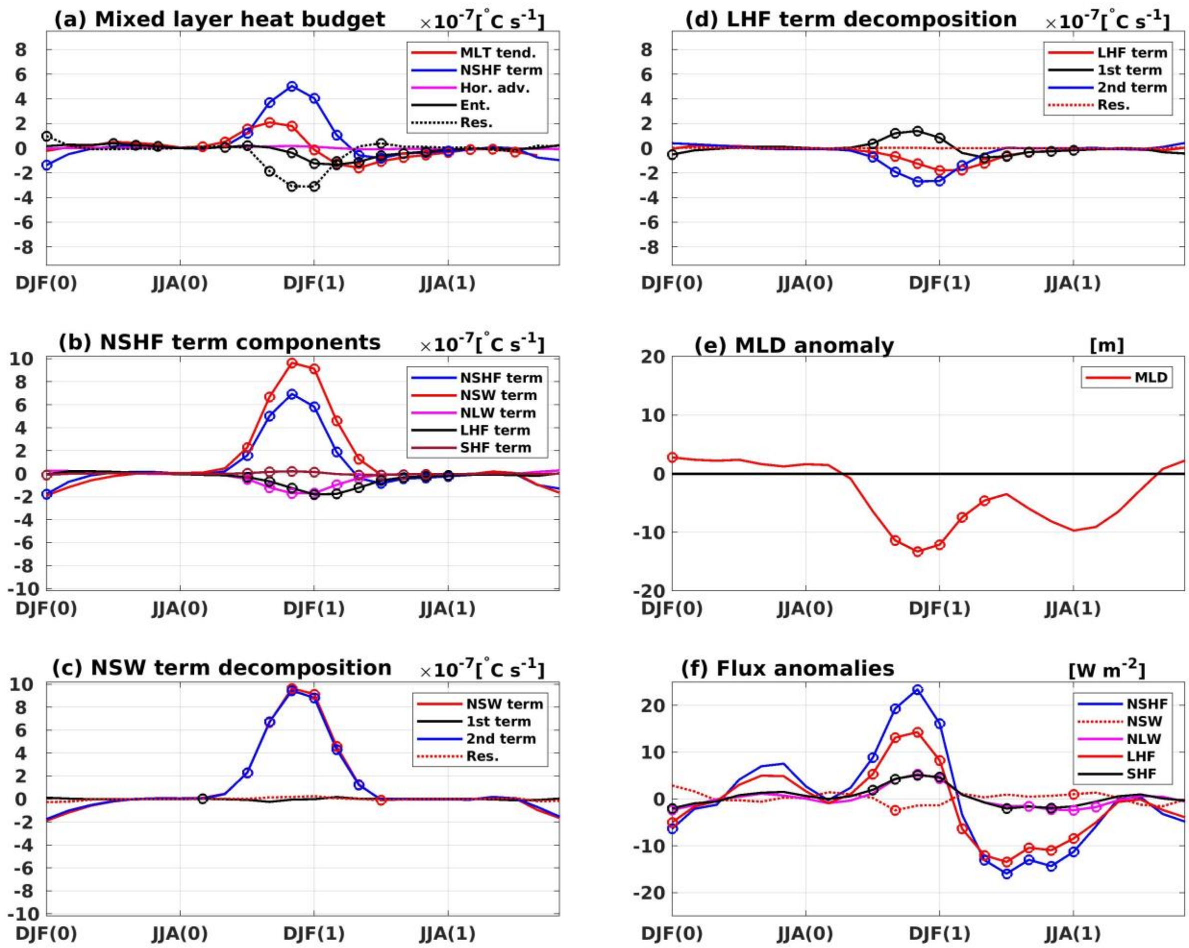

Figure 3. (a) Time series of composite anomalies of mixed layer heat budget terms in Eq. (3) ($\times 10^{-7}\ °C\ s^{-1}$) for the positive years. (b) Time series of components of net surface heat flux terms in the right-hand side of Eq. (3) ($\times 10^{-7}\ °C\ s^{-1}$) during positive years. Each term of Eq. (9) ($\times 10^{-7}\ °C\ s^{-1}$) corresponding to δQ for (c) the short wave radiation and (d) the latent heat flux during the positive years. (e) Time series of the MLD anomalies (in m), defined as δH in Eq. (9). (f) Time series of NSHF, NLW, NSW, SHF and LHF anomalies in W m^{-2} during the positive years. In (a) MLT tend., NSHF term, Hor. adv., Ent., and Res., indicate the tendency of MLT, net surface heat flux, horizontal advection, entrainment, and residual terms, respectively. In (b,c,d,f) NSW, NLW, LHF, and SHF indicate net shortwave radiation, net longwave radiation, latent heat flux, and sensible heat flux, respectively. To smooth the time series, a 3-month running mean is applied. Open circles show 90% significant anomalies using a two-tailed Student’s t-test.

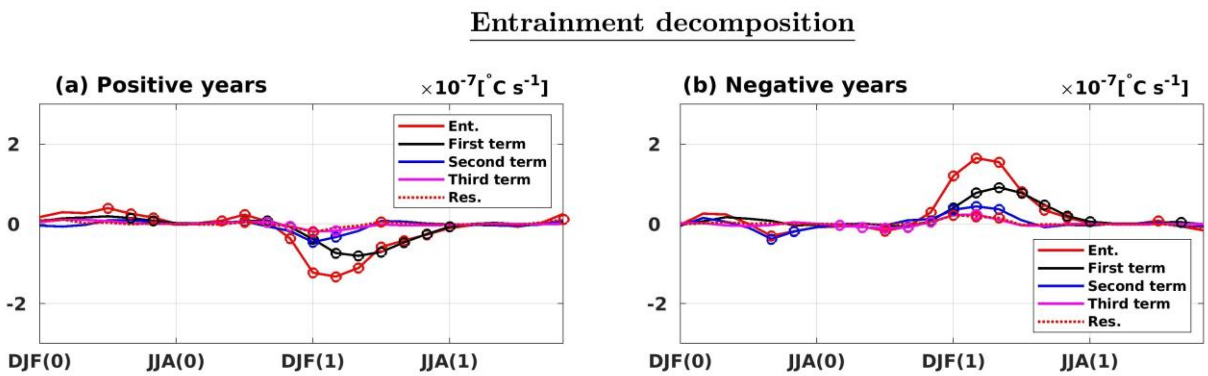

Figure 4. (a, b) Time series of anomalous contributions from each entrainment term ($\times 10^{-7}\ °C\ s^{-1}$) in Eq. (10) during the positive and negative years, respectively. To smooth the time series, we applied a 3-month running mean. Open circles show significant anomalies with 90% confidence levels using a two-tailed Student's *t*-test.

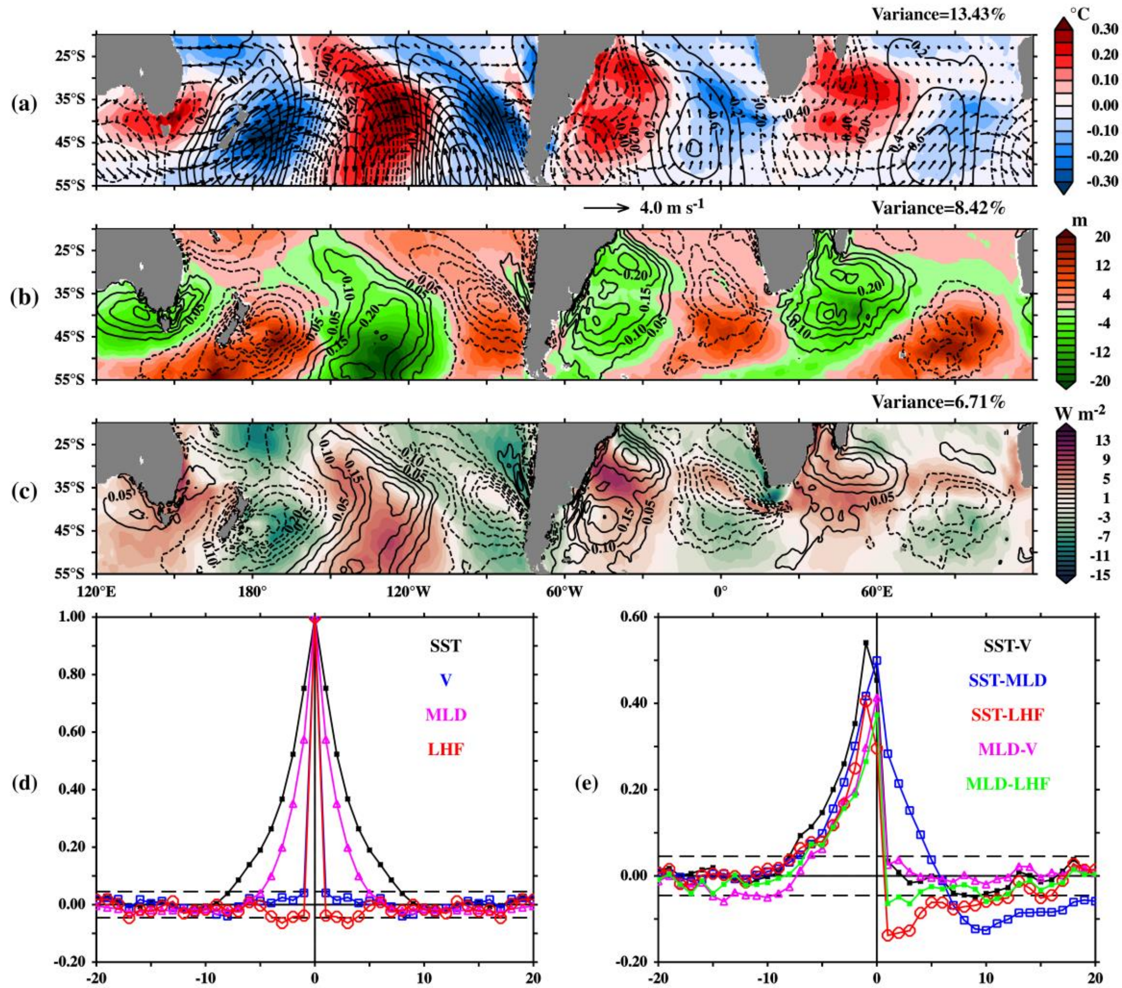

Figure 5. The second MCA mode between (a) SST anomaly (shaded; in °C) and 850 hPa horizontal wind anomaly (vectors; in m s^{-1}), meridional wind anomaly (contours, interval: 0.2 m s^{-1}) (b) SST anomaly (contours, interval: 0.05 °C) and MLD anomaly (shaded; in m) and (c) LHF anomaly (shaded; in W m^{-2}; positive downward) and SST anomaly (contours, interval: 0.05 °C). Variances are given on top-right of each panel (note: (a) is for variance between SST and meridional wind anomaly). Solid (dotted) contours represent positive (negative) values. (d) Auto-correlation and (e) cross-correlation of the second MCA time series among the SST anomaly, MLD anomaly, meridional wind anomaly (V), and LHF anomaly as indicated by the colors. The X-axis (Y-axis) represents the monthly lead/lag (correlation coefficients) and positive (negative) lag means the first variable is leading (lagging) the second. 99% statistical confidence level using Student's *t*-test are shown with dashed black lines.

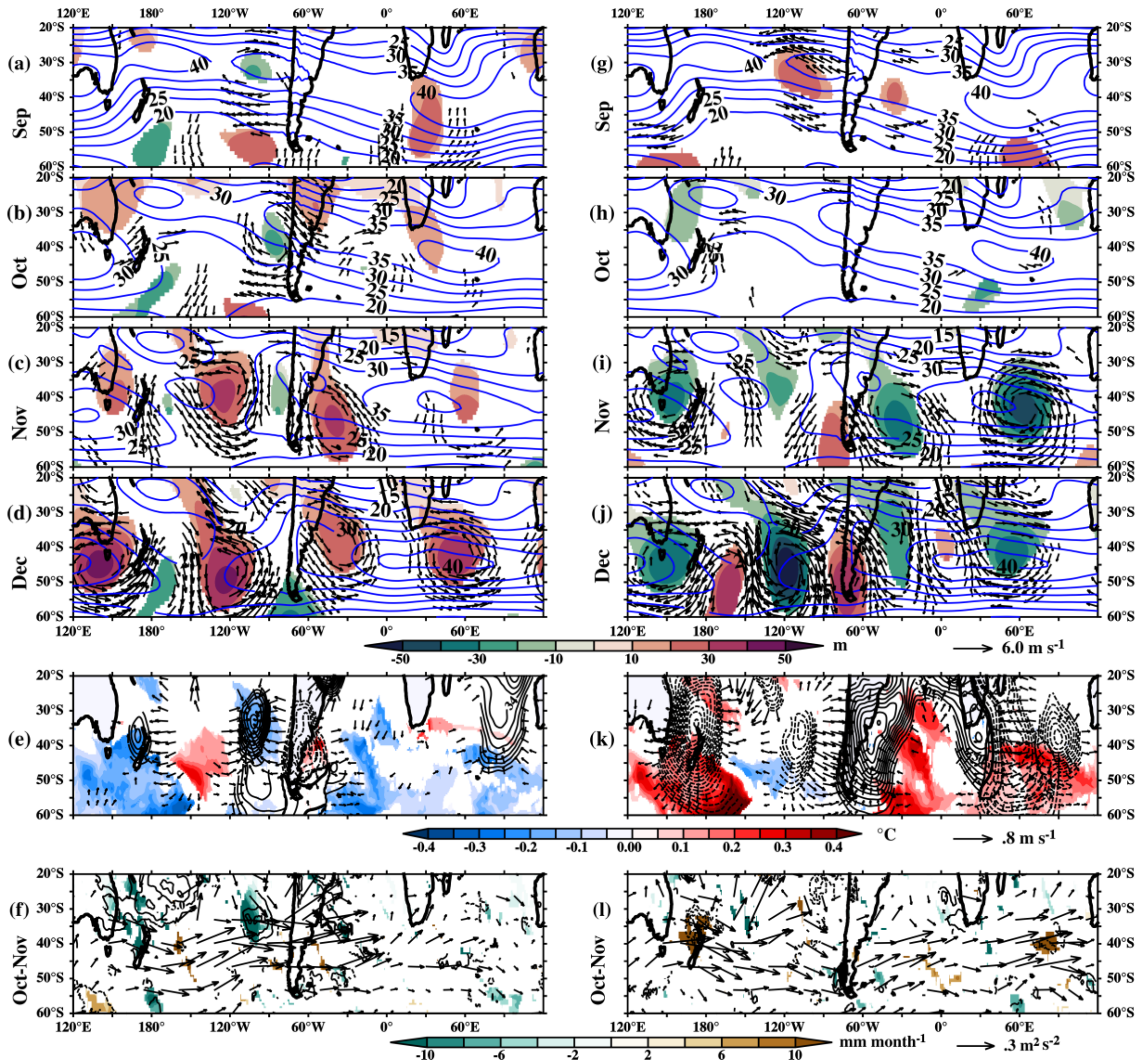

Figure 6. Monthly composites of anomalous 250 hPa geopotential height (shaded; in m) and wind (vectors; in m s^{-1}) for (a) September, (b) October, (c) November, and (d) December during the positive years. The blue contours of the zonal wind highlight the westerly jet. (e) SST anomaly (shaded) in October, velocity potential anomaly (contours, in $10^4\ m^2 s^{-1}$) and anomalous 250 hPa divergent wind (vectors; in m s^{-1}) during October-November, and (f) anomalous precipitation during October-November (shaded; in mm month^{-1}), Outgoing Longwave Radiation (black contours, in W m^{-2}) and WAF (vectors, in m^2 s^{-2}). (g-l) Monthly composites for the negative event years. Values exceeding 90% confidence levels using Student's *t*-test are plotted.

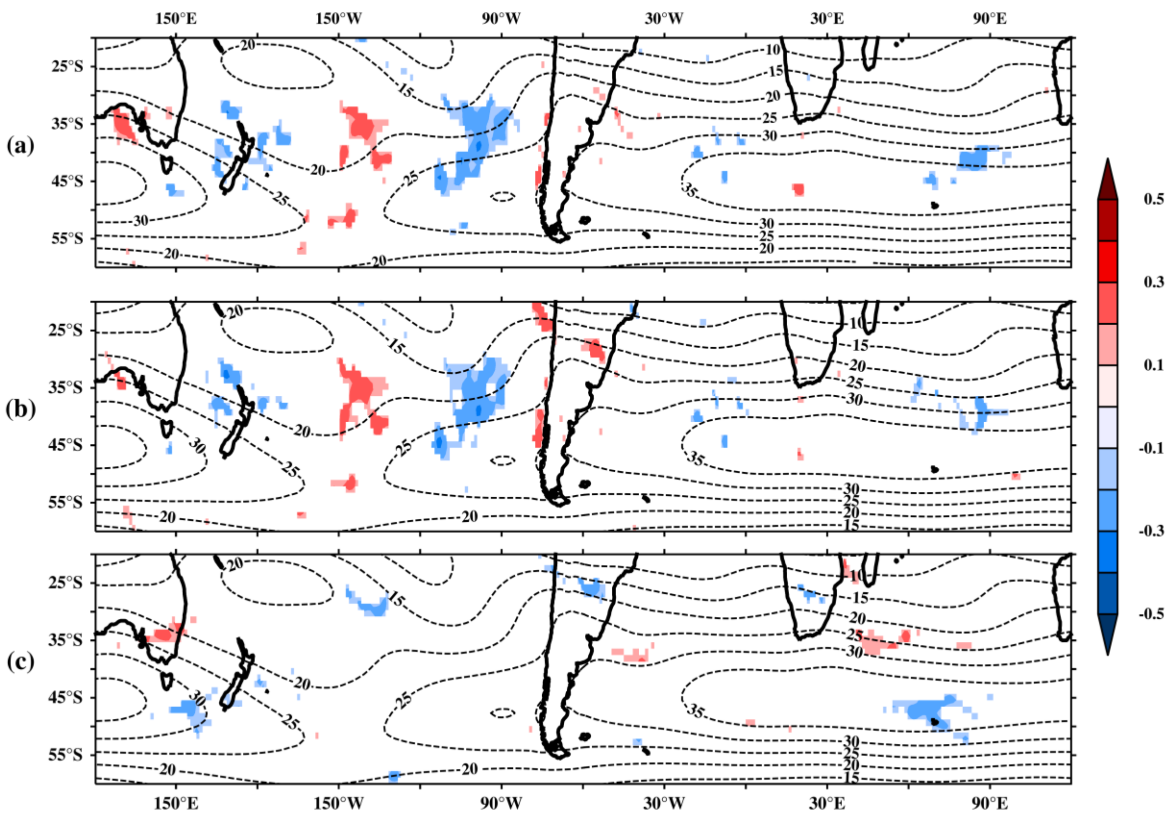

Figure 7. Correlation maps between the PC-2 in austral summer (December-February) and anomalous (a) RWS, (b) Term-1, and (c) Term-2 of Eq. (1) during October-November. Values exceeding 99% confidence level using Student's *t*-test are colored. The contour of black-dotted lines of zonal wind represents the westerly jet.

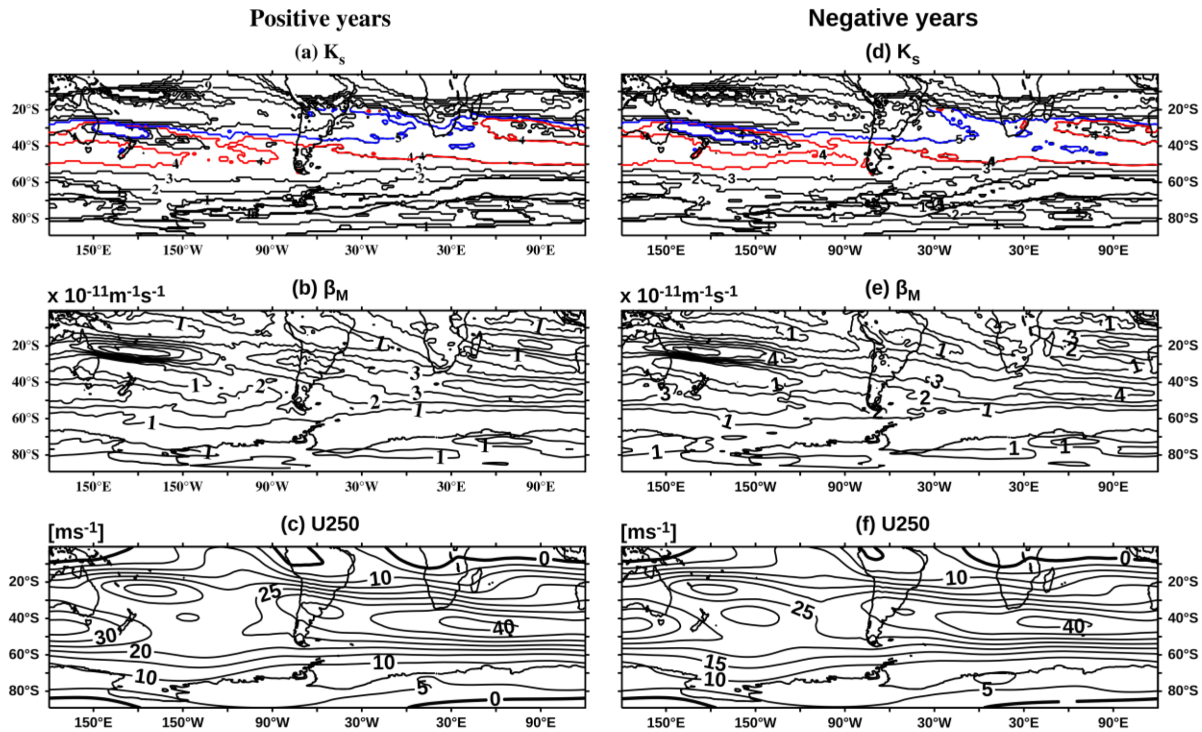

Figure 8. (a) Stationary Rossby wavenumber (K_s), (b) meridional gradient of absolute vorticity (β_M) ($\times 10^{-11}$ m^{-1} s^{-1}), and (c) zonal velocity at 250 hPa during November- January of the positive years. (d-f) Same as in (a-c), but for the negative years. The solid red (blue) contour in (a) and (d) correspond to stationary Rossby wavenumber 4 (5).

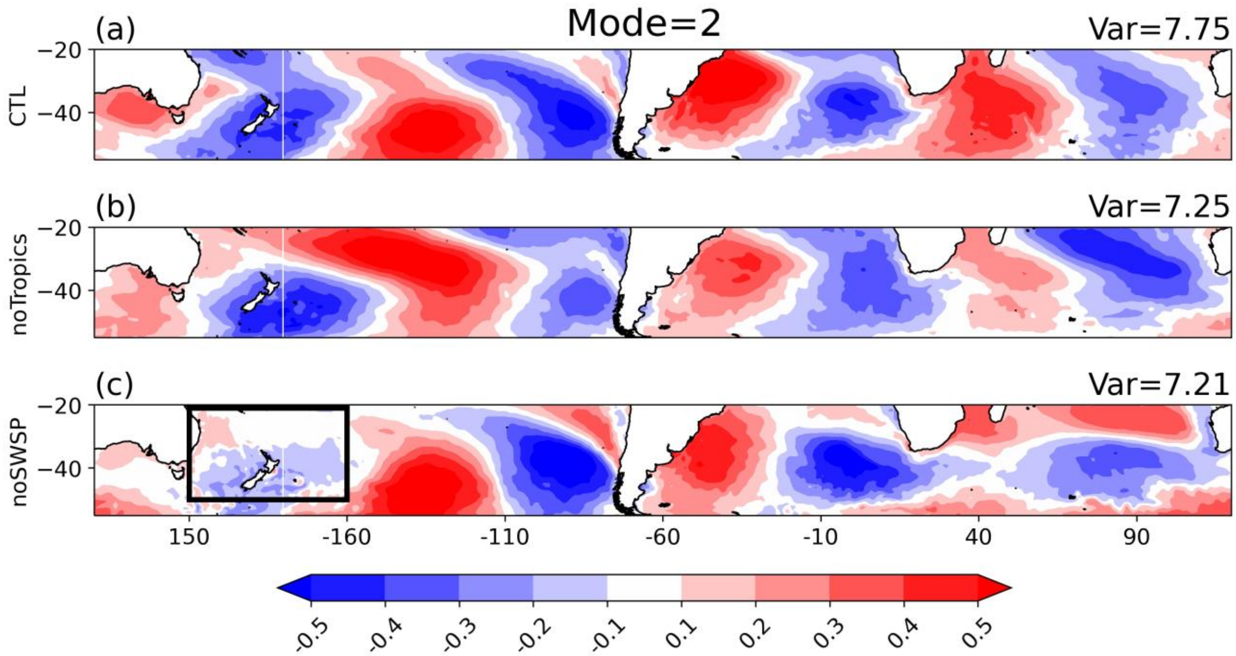

Figure 9. Spatial patterns of the second EOF mode of SST anomaly over the subtropical-midlatitude region (55°S-25°S) from (a) the CTL, (b) noTropics, and (c) noSWSP experiments. Here we used initial 70–yr simulation in the CTL experiment after removing the first 30 yr to have consistency with the noTropics and noSWSP experiments. Values in the top right explain their variance. The black rectangle box in (c) shows the SST-nudging area in the noSWSP experiment.

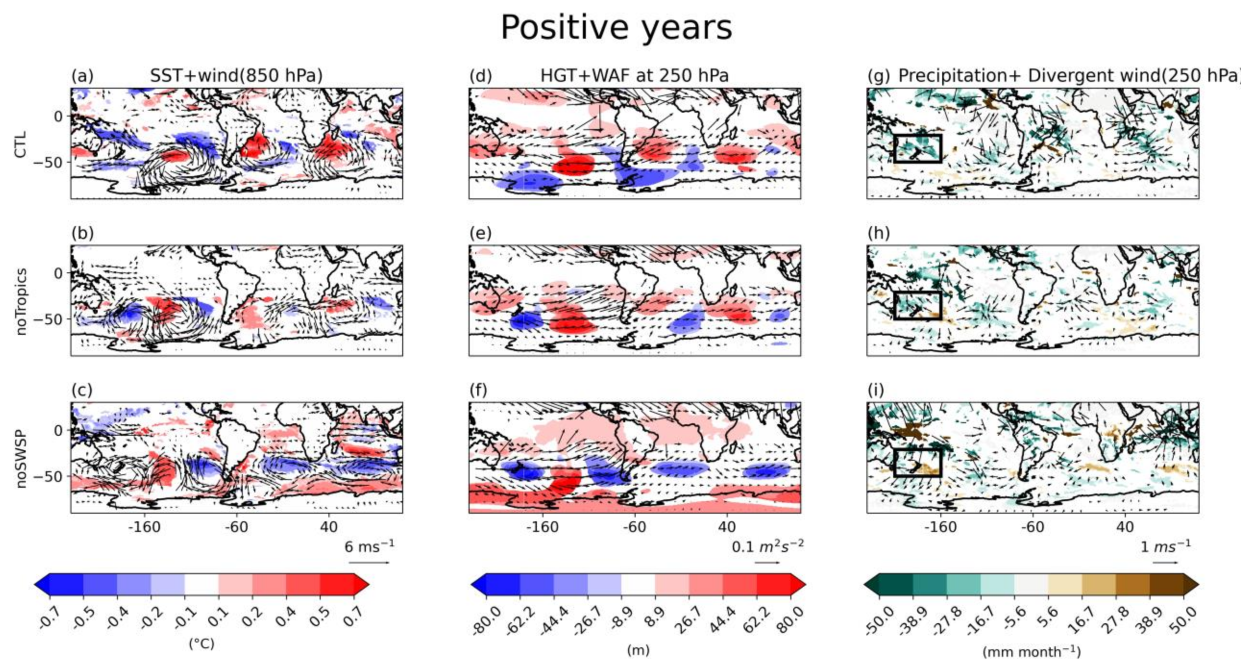

Figure 10. (a-c) Composite maps of SST (shaded; in °C) and 850 hPa wind anomalies (vectors; in m s^{-1}) for the CTL, noTropics, and noSWSP experiments during positive years. The middle panel (d-f) is similar to the left panel but for anomalous geopotential height (shaded; in m) and wave activity flux (vectors; in m^2 s^{-2}) at 250 hPa. Similarly, the right panel (g-i) is for precipitation (shaded; in mm month^{-1}) and 250 hPa divergent wind anomalies (vectors; in m s^{-1}). HGT and WAF indicate the geopotential height and wave activity flux. Values not satisfying 90% confidence level in a two-tailed Stundent's *t*-test are masked out. The black rectangle box in (c) shows the SST-nudging area in the noSWSP experiment.

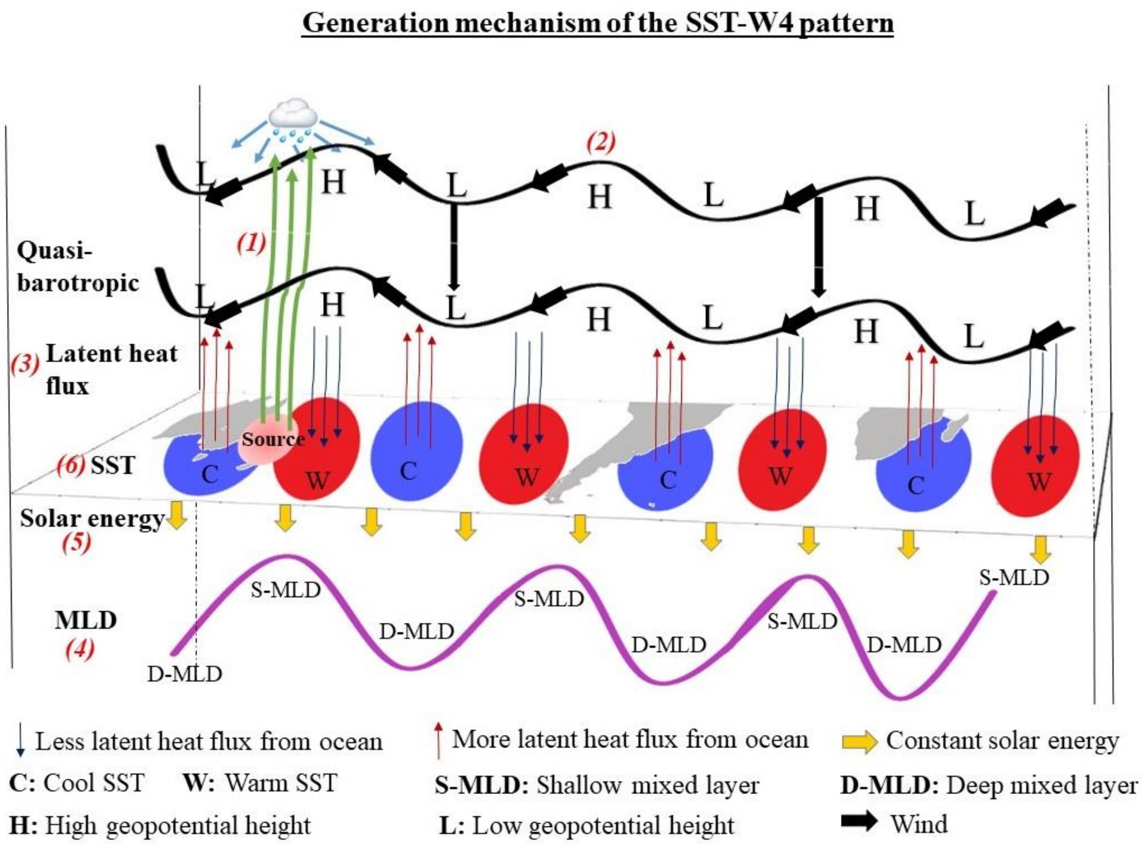

Figure 11. Schematic diagram describing the generation mechanism of the SST-W4 pattern in the subtropical-midlatitude Southern Hemisphere.

Table:

	SON	OND	NDJ	DJF	JFM
Monin-Obukhov depth	-16.64	**-30.04**	**-35.29**	**-32.29**	-10.07
Wind stirring	-0.01	-0.19	**-0.28**	**-0.21**	0.5

Flux	-16.5	**-29.95**	**-35.22**	**-32.21**	-10.7
Res.	-0.13	0.1	0.21	0.13	0.13

Table 1. Monin-Obukhov depth anomaly (in m) and anomalous contributions from surface flux, wind stirring, and residual terms in Eq. (7) during September-November, October-December, November-January, December-February, and January-March of the positive years. Bold letters show significant anomalies with 90% confidence levels using a two-tailed Student's *t*-test.

Supporting Information for

Southern Hemisphere Circumpolar Wavenumber-4 Pattern Simulated in SINTEX-F2 Coupled Model

Balaji Senapati[1,2], Yushi Morioka[3], Swadhin K. Behera[3], and Mihir K. Dash[1]

[1] Centre for Ocean, River, Atmosphere and Land Sciences, Indian Institute of Technology Kharagpur, Kharagpur, West Bengal, India

[2] Department of Meteorology, University of Reading, Reading, UK

[3] Application Laboratory, VAiG, Japan Agency for Marine-Earth Science and Technology, Yokohama, Kanagawa, Japan

Contents of this file

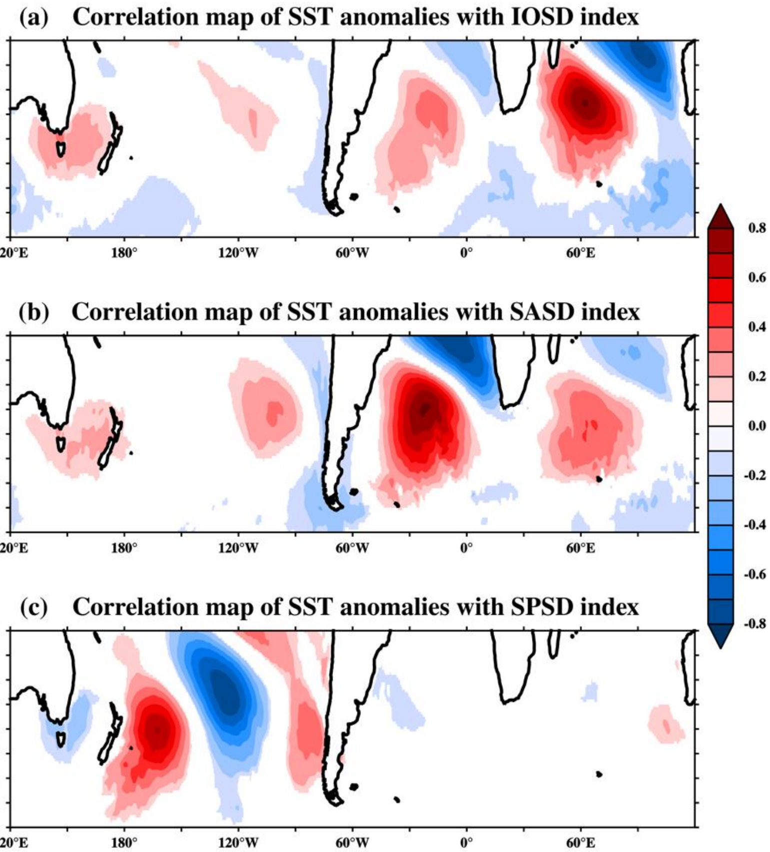

Figure S1. Correlation maps of SST anomalies with (a) IOSD, (b) SASD, and (c) SPSD indices. Values exceeding a 99% confidence level of the correlation coefficients using Student's *t*-test are colored.

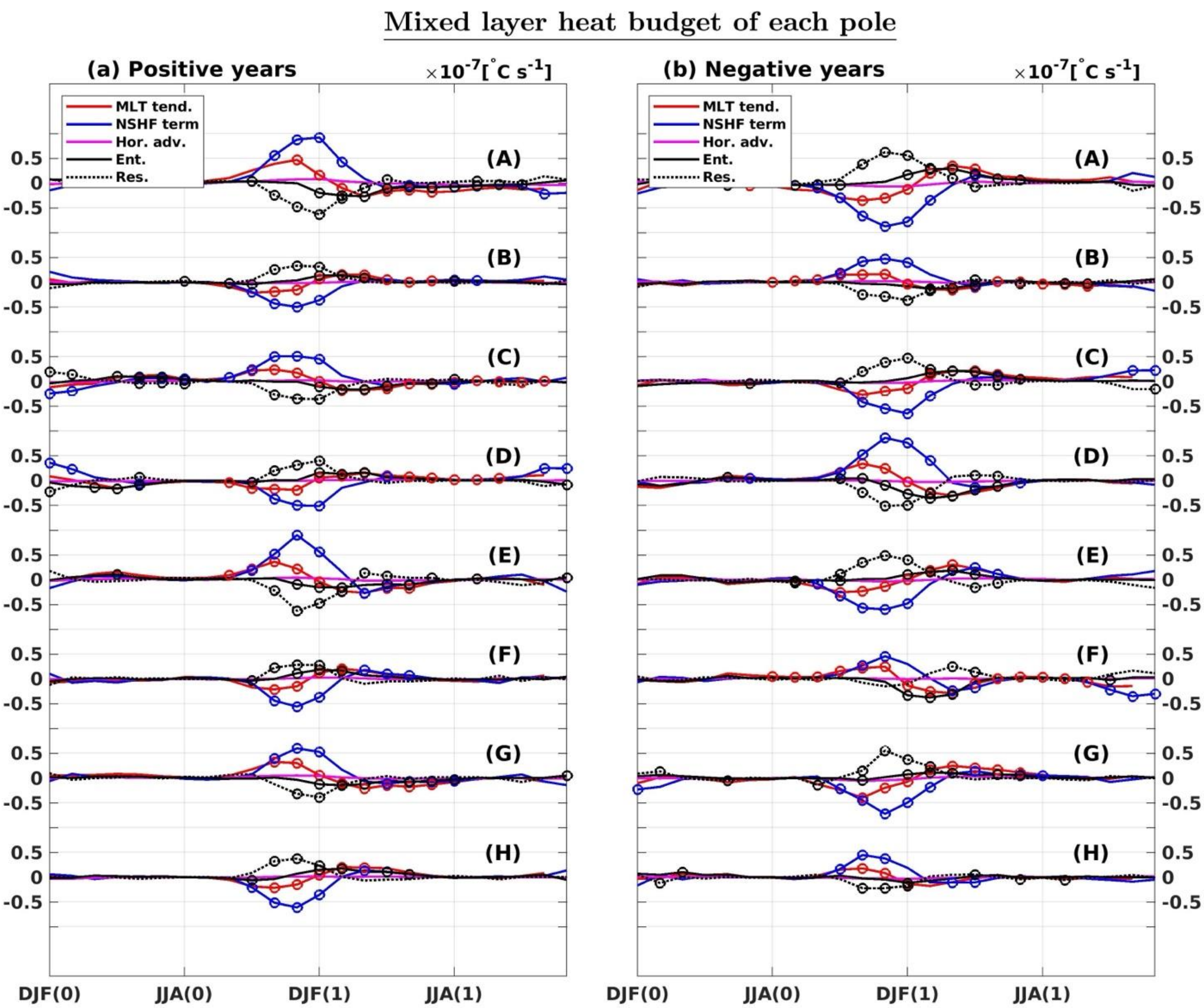

Figure S2. Same as in Fig. 3a, but for each of the rectangular boxes (A to H) defined in Fig. 2a for (a) positive and (b) negative years.

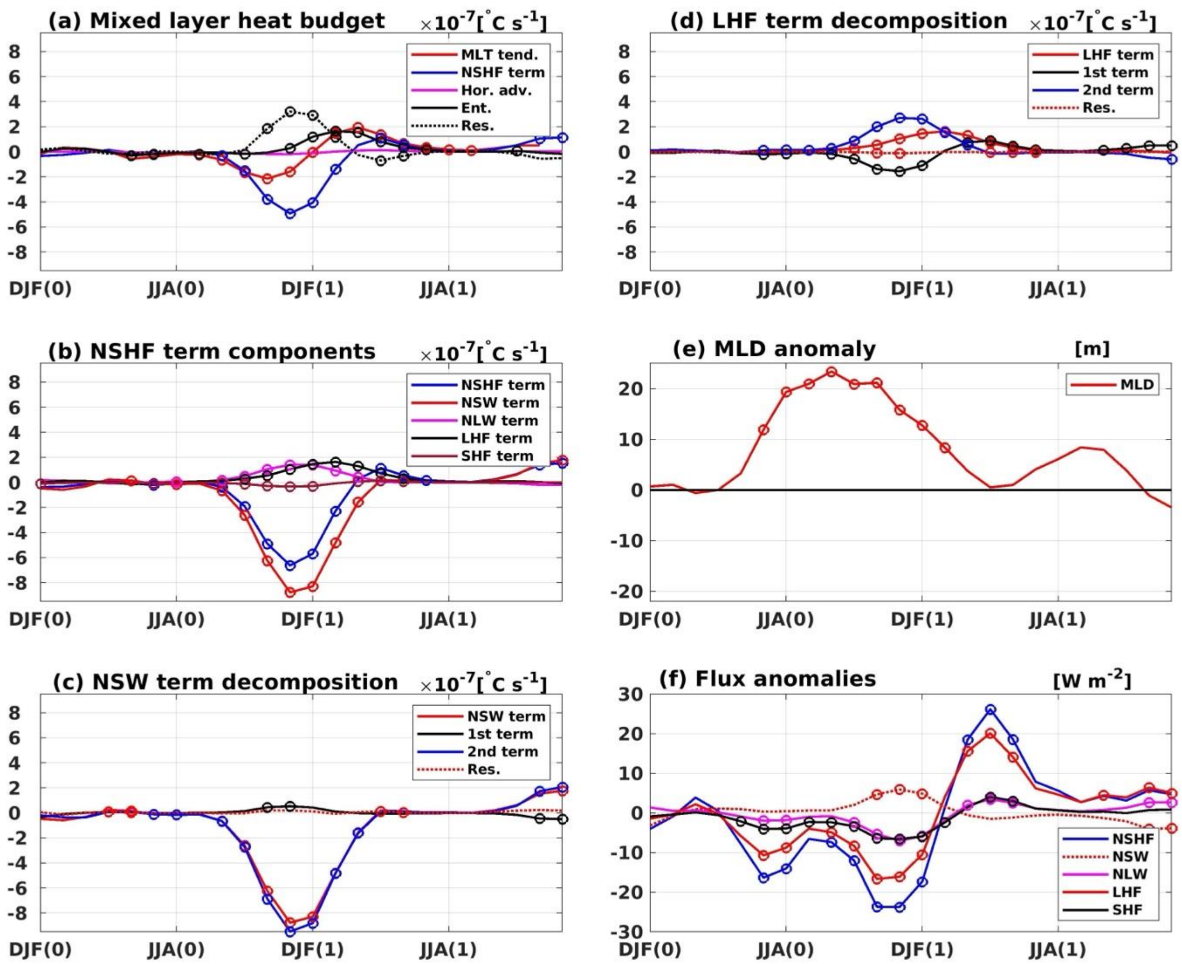

Figure S3. Same as in Fig. 3 but for the negative years.

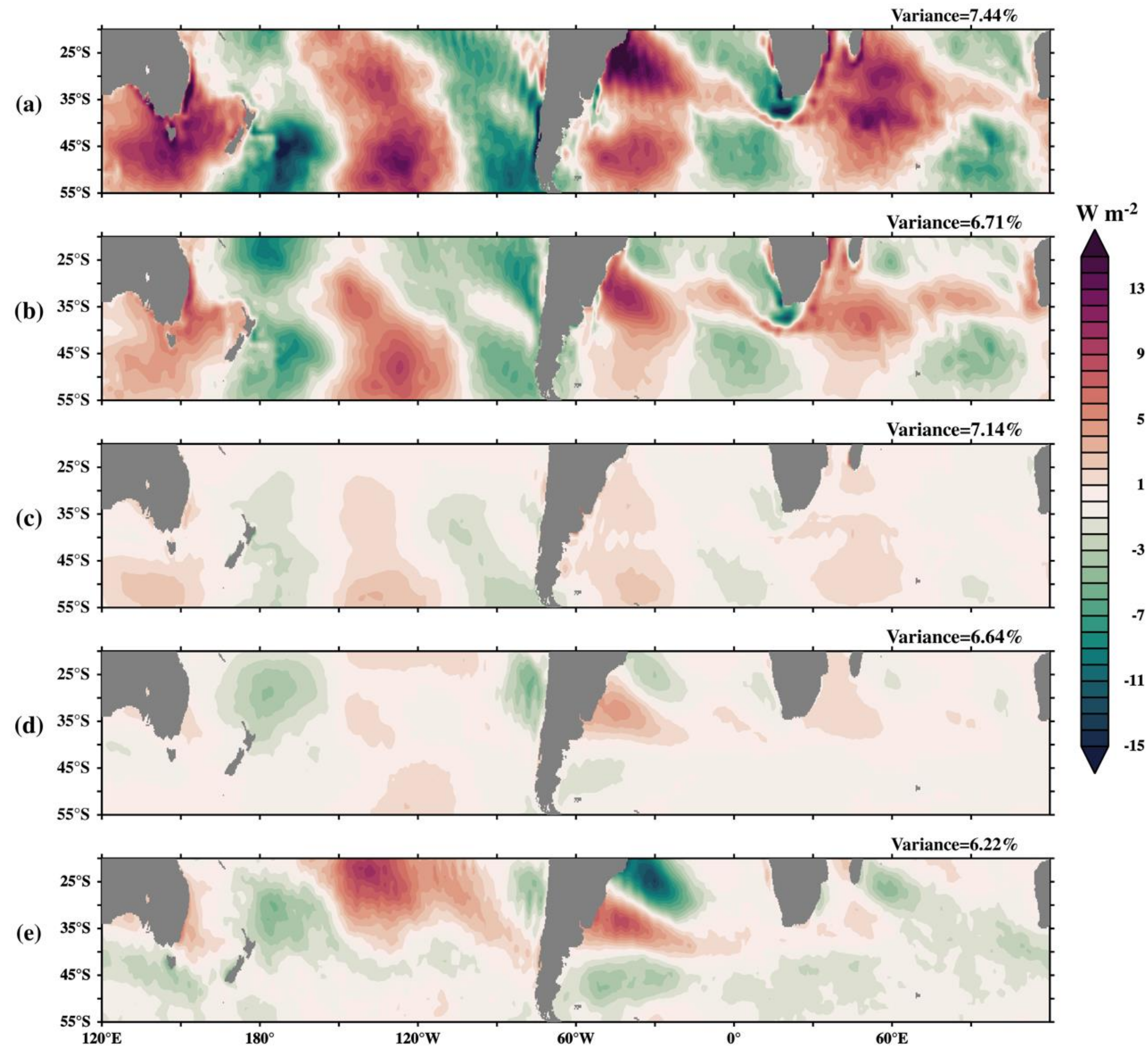

Figure S4**.** The second MCA mode between SST anomaly and (a) net surface heat flux anomaly, (b) latent heat flux anomaly, (c) sensible heat flux anomaly, (d) longwave radiation anomaly, and (e) shortwave radiation anomaly. Positive values represent downward heat fluxes to warm the ocean.

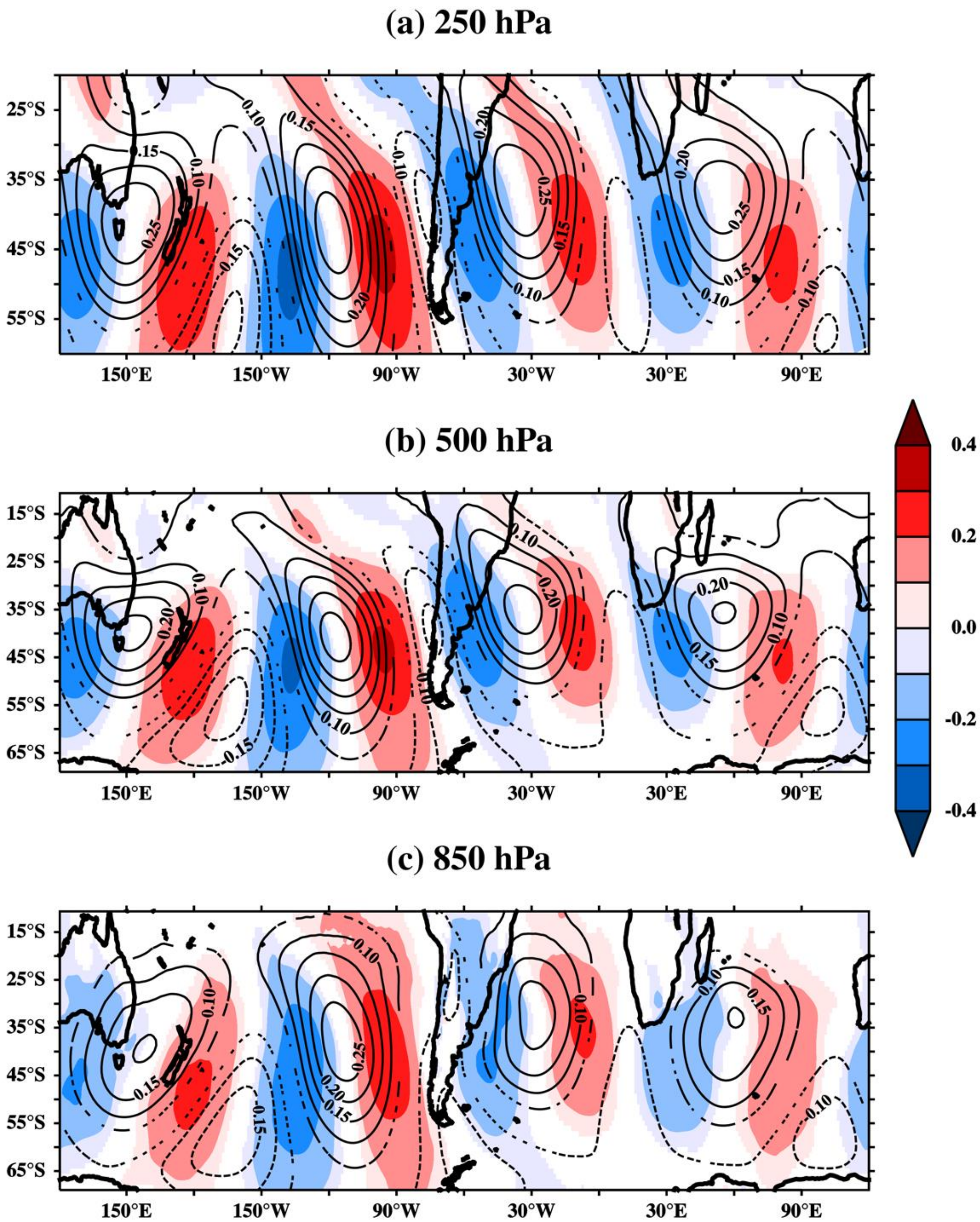

Figure S5. Correlation maps of PC-2 with meridional wind anomalies (shaded) and geopotential height anomalies (contour interval: 0.05) at (a) 250 hPa, (b) 500 hPa, and (c) 850 hPa. Values exceeding a 99% confidence level of the correlation coefficients using Student's *t*-test are plotted.

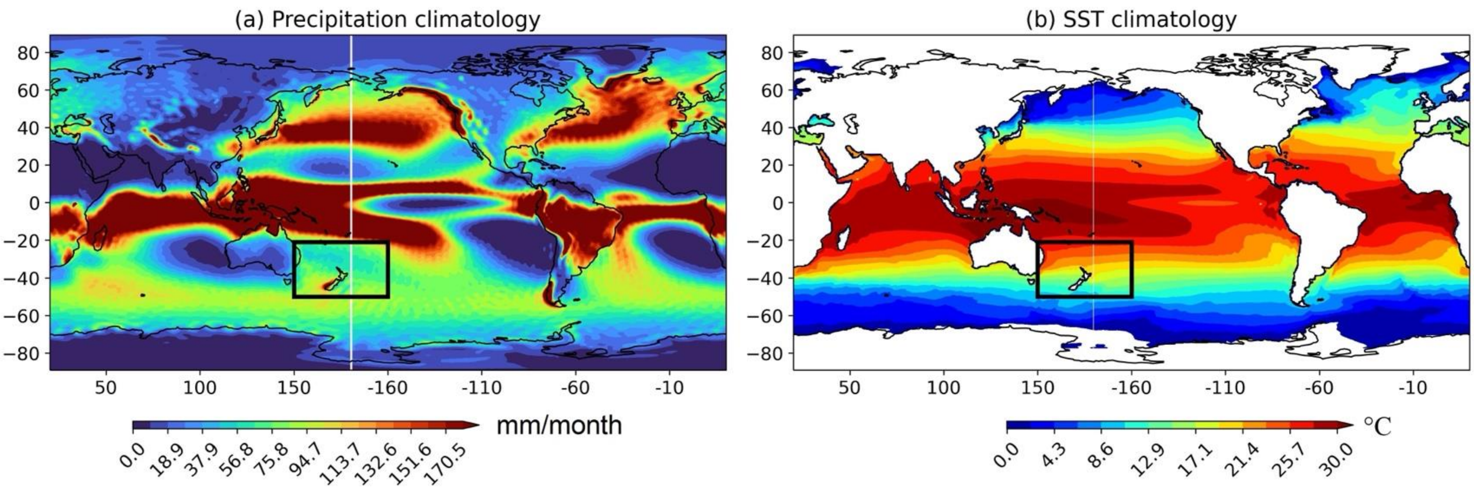

Figure S6. Climatologies of (a) precipitation and (b) SST during austral summer (December-February). Black rectangle box shows the SST-nudging area in the noSWSP experiment.

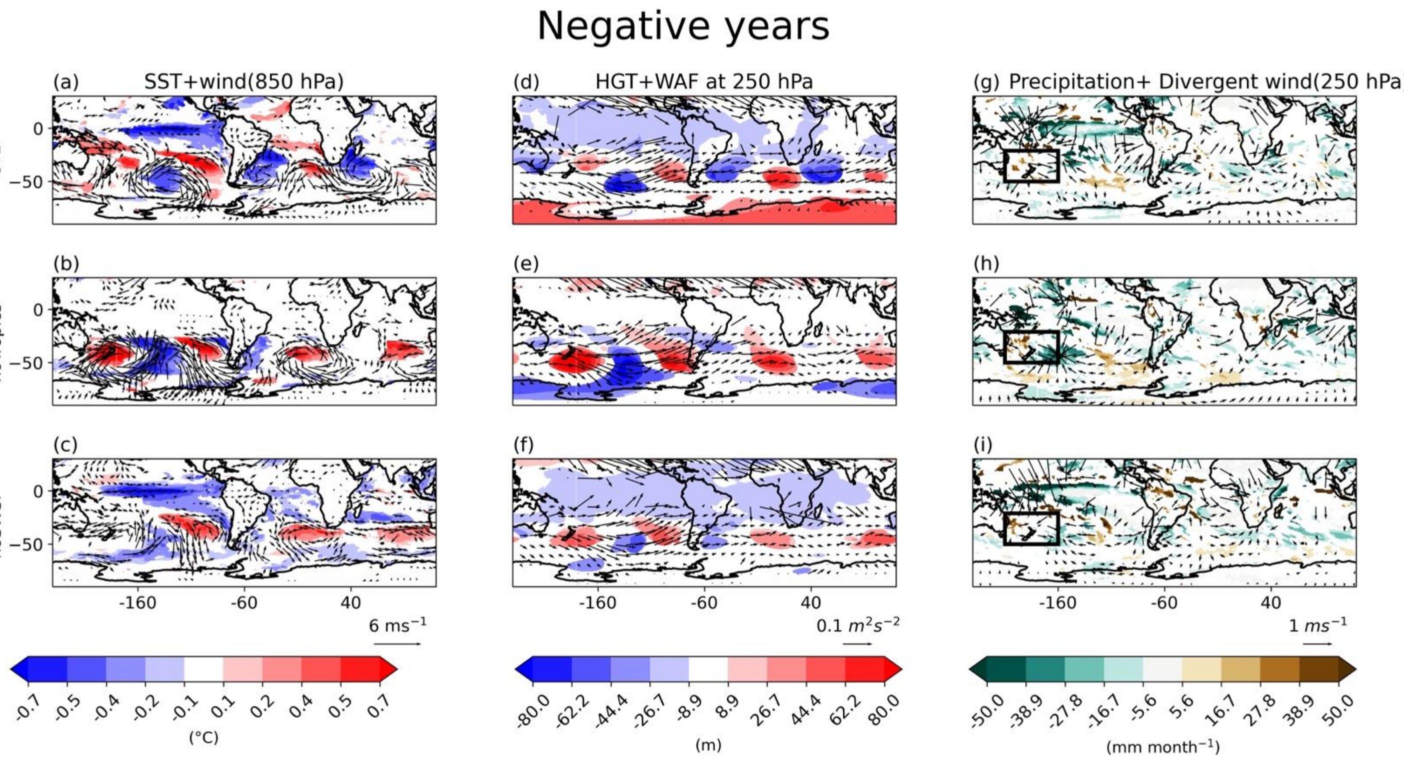

Figure S7. Same as in Fig. 10 but for the negative years.

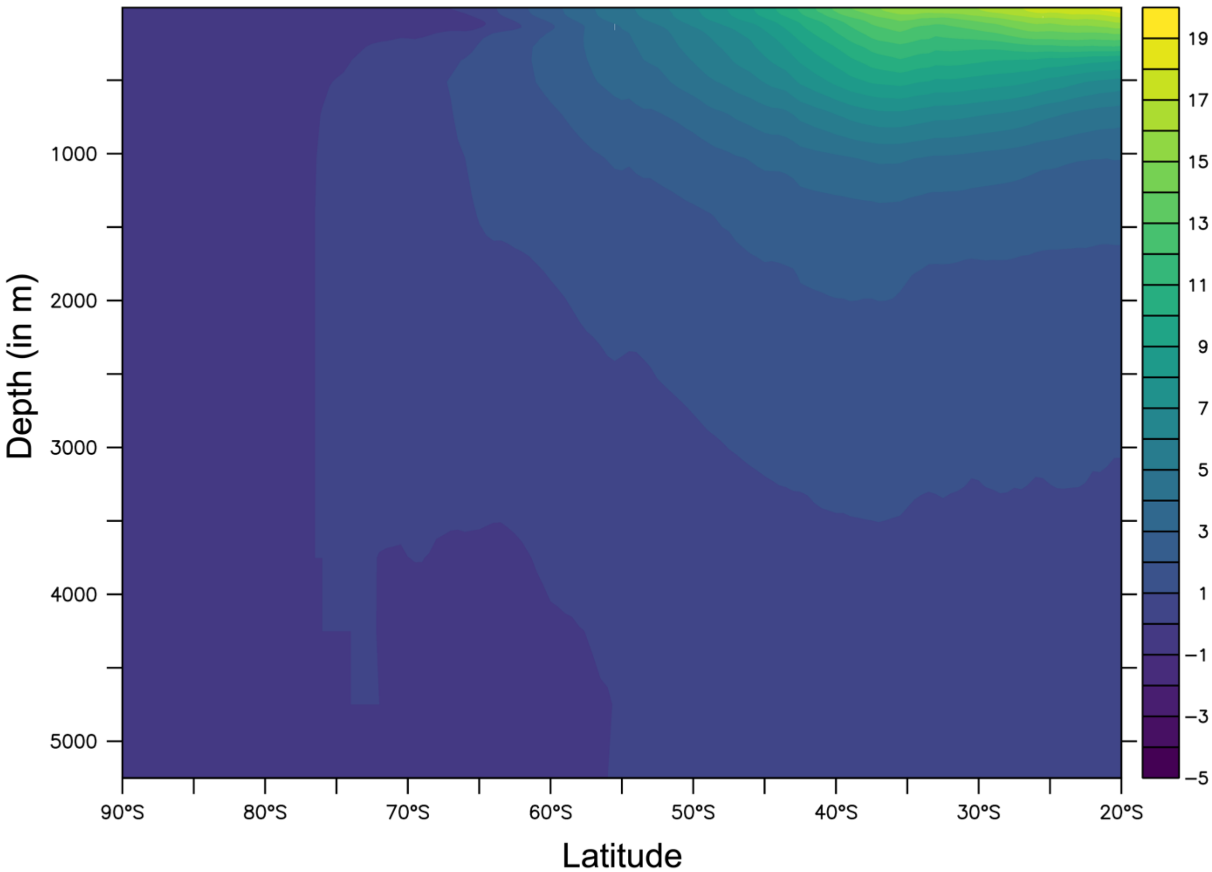

Figure S8. Climatology of zonal mean potential temperature in the ocean.

	SON	OND	NDJ	DJF	JFM
Monin-Obukhov depth	15.55	**37.11**	**39.06**	**34.57**	12.17
Wind stirring	0.57	**0.45**	**0.28**	**0.19**	**-0.88**
Flux	15.42	**37.06**	**38.98**	**34.49**	11.99
Res.	-0.44	-0.4	-0.2	-0.11	1.06

Table S1. Same as in Table 1 but for negative years.

MCA 2^{nd} Mode	SST-V	SST-MLD	SST-LHF	SST-SHF	SST-NLW	SST-NSW	SST-NSHF
Variance	13.43%	8.42%	6.71%	7.14%	6.64%	6.22%	7.44%
Error	0.66	0.41	0.33	0.35	0.33	0.3	0.36
Significance	Significant	Significant	Significant	Significant	Significant	Significant	Significant

Table S2. Significance of 2^{nd} mode of MCA analysis using North et al. (1982) criteria.